

A Plug-and-Play Method for Guided Multi-contrast MRI Reconstruction based on Content/Style Modeling

Chinmay Rao^{a,*}, Matthias van Osch^a, Nicola Pezzotti^{b,c}, Jeroen de Bresser^a, Mark van Buchem^a, Laurens Beljaards^a, Jakob Meineke^d, Elwin de Weerd^e, Huangling Lu^a, Mariya Doneva^d, Marius Staring^a

^a*Department of Radiology, Leiden University Medical Center, Leiden, The Netherlands*

^b*Cardiologs, Paris, France*

^c*Department of Mathematics and Computer Science, Eindhoven University of Technology, Eindhoven, The Netherlands*

^d*Philips Innovative Technologies, Hamburg, Germany*

^e*Philips, Best, The Netherlands*

Abstract

Since multiple MRI contrasts of the same anatomy contain redundant information, one contrast can guide the reconstruction of an undersampled subsequent contrast. To this end, several end-to-end learning-based guided reconstruction methods have been proposed. However, a key challenge is the requirement of large paired training datasets comprising raw data and aligned reference images. We propose a modular two-stage approach that does not require any k-space training data, relying solely on image-domain datasets, a large part of which can be unpaired. Additionally, our approach provides an explanatory framework for the multi-contrast problem based on the shared and non-shared generative factors underlying two given contrasts. A content/style model of two-contrast image data is learned from a largely unpaired image-domain dataset and is subsequently applied as a plug-and-play operator in iterative reconstruction. The disentanglement of content and style allows explicit representation of contrast-independent and contrast-specific factors. Consequently, incorporating prior information into the reconstruction reduces to a simple replacement of the aliased content of the reconstruction iterate with high-quality content derived from the reference scan. Combining this component with a data consistency step and introducing a general corrective process for the content yields an iterative scheme. We name this novel approach PnP-CoSMo. Various aspects like interpretability and convergence are explored via simulations. Furthermore, its practicality is demonstrated on the public NYU fastMRI DICOM dataset, showing improved generalizability compared to end-to-end methods, and on two in-house multi-coil raw datasets, offering up to 32.6% more acceleration over learning-based non-guided reconstruction for a given SSIM.

Keywords: MRI reconstruction, multi-modal, content/style decomposition, plug-and-play

1. Introduction

Magnetic resonance imaging (MRI) is an invaluable medical imaging modality due to the high-quality scans it delivers, the variety of complementary information it can capture, and its lack of radiation-related risks, leading to its wide usage in clinical practice. However, its central limitation is the inherently slow data acquisition process. The raw sensor data is acquired in the frequency domain, or k-space, from which the image is reconstructed. Over the last 25 years, advancements such as parallel imaging (Pruessmann et al., 2001; Griswold et al., 2002), compressed sensing (CS) (Lustig et al., 2007), and deep learning reconstruction (Aggarwal et al., 2018; Pezzotti et al., 2020) have enabled considerable speedups by allowing sub-Nyquist

*c.s.rao@lumc.nl

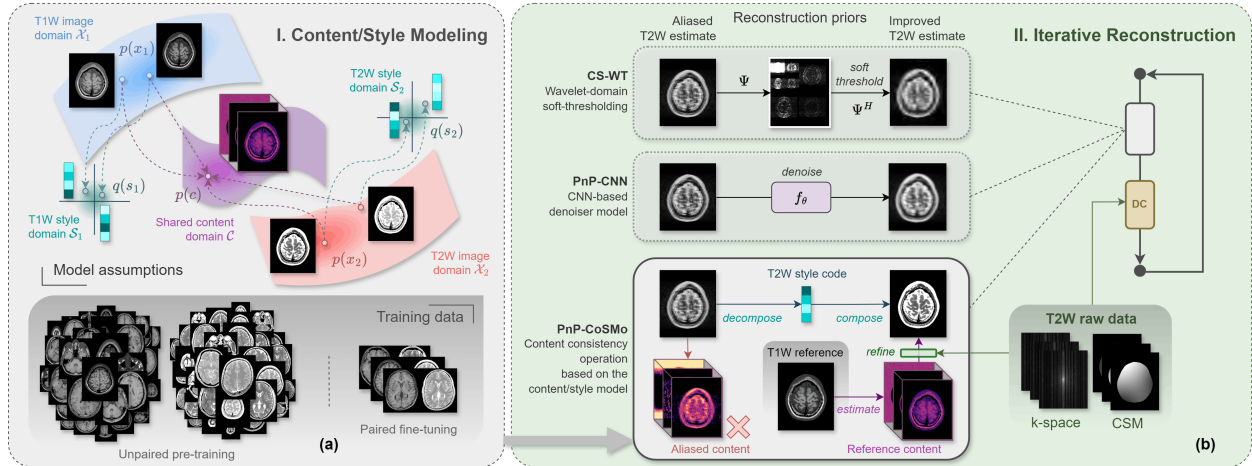


Figure 1: Our two-stage approach to guided reconstruction. (a) The first stage learns a content/style model of two-contrast MR image data offline. No k-space data is required in this stage. We assume that the two image domains \mathcal{X}_1 and \mathcal{X}_2 can be decomposed into a shared content domain \mathcal{C} and separate style domains \mathcal{S}_1 and \mathcal{S}_2 . This model is learned in two stages – an unpaired pre-training stage and a paired fine-tuning stage, both requiring only image data. (b) The reconstruction stage applies the content/style model as a *content consistency operator* (bottom) within an ISTA-based iterative scheme. Given an aligned reference image, guidance is introduced into the reconstruction by simply replacing its aliased content with content derived from the reference. The "refine" block denotes a content refinement update, which iteratively corrects for inconsistencies between the reference content and the measured k-space data, improving the effectiveness of the content consistency operator. DC denotes data consistency. For comparison, two other reconstruction priors are shown, namely wavelet-domain soft-thresholding (top) and CNN-based denoising (middle) used in CS and PnP-CNN algorithms, respectively.

k-space sampling and relying on computationally sophisticated reconstruction. These techniques have subsequently been implemented on commercial MRI systems and have demonstrated (potential) improvements in clinical workflow (Seow et al., 2024).

A clinical MRI session typically involves the acquisition of multiple scans of the same anatomy through the application of different MR pulse sequences, exhibiting different contrasts. Because these scans are different reflections of the same underlying reality, they share a high degree of shared structure. However, currently deployed clinical protocols acquire and reconstruct each scan as an independent measurement, not leveraging the information redundancy across scans. There is, therefore, an opportunity to further optimize MRI sessions by exploiting this shared information. On the reconstruction side, multi-contrast methods have addressed this problem by introducing the shared information into the reconstruction phase to allow higher levels of k-space undersampling. In the simplest case of two contrasts, multi-contrast reconstruction can be classified into two types: (a) guided reconstruction, where an existing high-quality reference scan is used to guide the reconstruction of an undersampled second scan (Ehrhardt and Betcke, 2016; Weizman et al., 2016; Zhou and Zhou, 2020) and (b) joint reconstruction, where both contrasts are undersampled and are reconstructed simultaneously (Bilgic et al., 2011; Huang et al., 2014; Kopanoglu et al., 2020). In this work, we consider the problem of guided reconstruction, assuming no inter-scan motion between reference and target scans.

The guided reconstruction problem entails using the local structure of the reference scan as a prior to complement the undersampled k-space measurements of the target scan. This problem has been formulated in different ways, ranging from conventional CS (Ehrhardt and Betcke, 2016; Weizman et al., 2016) to end-to-end learning with unrolled networks (Zhou and Zhou, 2020; Yang et al., 2020; Pooja et al., 2022; Lei et al., 2023) and, more recently, diffusion model-based Bayesian maximum *a posteriori* estimation (Levac et al., 2023). Most end-to-end approaches, although more powerful than earlier hand-crafted ones, suffer from the main drawback of requiring large paired training datasets consisting of the target image and its k-space together with an aligned reference image, thereby limiting their application on real-world MR data. We address this issue by proposing a plug-and-play reconstruction method that splits the problem

into a purely image-domain learning sub-problem and an iterative reconstruction sub-problem. The learning problem leverages ideas from content/style decomposition, thereby offering a degree of interpretability to our approach. To the best of our knowledge, ours is the first work that thoroughly explores content/style-based generative modeling for multi-contrast MRI reconstruction.

In recent years, image-to-image translation has found application in the direct estimation of one MR contrast from another (Dar et al., 2019; Yurt et al., 2021; Denck et al., 2021; Atli et al., 2024). While these methods are attractive due to their lack of dependence on k-space data, viewed in the light of MR physics, cross-contrast translation takes an extreme stance by not explicitly taking into account contrast-specific sensitivities and relying solely on the prior contrast. Hence, in the context of MR image formation, cross-contrast translation, by itself, can only provide a part of the information about the target image as data acquisition via MR sequences is necessary to obtain new information about the anatomy. That being said, literature on unpaired image translation provides a repertoire of useful tools such as joint generative modeling of two-domain image data (Liu et al., 2017; Huang et al., 2018), which can be adopted to complement image reconstruction. We observe that methods such as MUNIT (Huang et al., 2018) can be applied to learn semantically meaningful representations of contrast-independent and contrast-specific information as content and style, respectively, without the need for paired image-domain training data.

Plug-and-play (PnP) methods are an emerging paradigm for solving inverse problems in computational imaging. The main research line (Ahmad et al., 2020; Kamilov et al., 2023) has focused on learning CNN-based denoising models on image-domain data and applying them as functions replacing proximal operators in iterative algorithms like ISTA and ADMM, demonstrating improved image recovery. An advantage of this approach is the decoupling of the learning problem of image modeling from the inverse problem of image reconstruction, thereby simplifying model training and improving generalizability across different acceleration factors, undersampling patterns, etc. With this design pattern in mind, we combine content/style image modeling and iterative reconstruction in a PnP-like framework.

We first leverage semantic content/style modeling to learn explicit representations of contrast-independent and contrast-specific components from two-contrast MR image data. This training process is independent of the reconstruction problem and can be performed using unpaired images. We then make the interesting observation that in multi-contrast MR images, the style information tends to localize in the center of the k-space, allowing for an accurate style estimation from an undersampled image. Since the content of the reconstructing image, which is the remaining piece of information and is contrast-independent, is supplied by the reference image, one can compose a de-aliased estimate of the reconstruction from the undersampled image in a single step. We term this the *content consistency operation*, which forms the basis of our iterative reconstruction algorithm PnP-CoSMo (Plug-and-Play method based on Content/Style Modeling) (Rao et al., 2024). An overview of our approach is shown in Fig. 1. While the PnP-based decoupling of image modeling and image reconstruction simplifies the training process and allows the two stages to be analyzed separately, a further level of decoupling offered by content/style disentanglement offers additional modularity and an intuitive guidance mechanism for the reconstruction. Specifically, our contributions are four-fold:

1. We show that unpaired image-domain training can be used to learn disentangled contrast-independent and contrast-specific representations, followed by a fine-tuning strategy that refines the content representation using a modest amount of paired image-domain data.
2. With this content/style model as the basis, we define a *content consistency operator* capable of removing severe undersampling artifacts from the reconstructing image, given the corresponding reference image.
3. Developing this idea further and incorporating a corrective process for the content, we propose PnP-CoSMo, a modular algorithm for guided reconstruction combining the flexibility of the plug-and-play approach with the semantic interpretability of content/style decomposition.
4. Through comprehensive experiments, we (a) shed light on several properties of PnP-CoSMo such as convergence and robustness, (b) demonstrate its equivalent performance and superior generalizability compared to state-of-the-art end-to-end models, (c) demonstrate its applicability on real-world raw data, and (d) evaluate its potential clinical utility with a preliminary radiological task.

2. Related work

2.1. Reconstruction methods for accelerated MRI

Techniques for accelerating MRI by k-space undersampling go back to compressed sensing (CS) (Lustig et al., 2007), which combines random sampling with sparsity-based iterative denoising, most commonly implemented based on the ISTA (Chambolle et al., 1998) or ADMM ((Boyd et al., 2011)) family of algorithms. Most modern deep learning-based reconstruction methods focus on improving the denoising part. Plug-and-play (PnP) methods (Ahmad et al., 2020; Kamilov et al., 2023) replace the proximal operator in ISTA and ADMM with off-the-shelf denoisers such as a learned convolutional denoising model. Unrolled networks (Schlemper et al., 2017; Aggarwal et al., 2018; Pezzotti et al., 2020) extend this idea by casting the entire iterative algorithm into one large network, trained end-to-end. This makes them more adaptive to factors such as sampling pattern and acceleration, although at a cost of generalizability (Ahmad et al., 2020).

One of the earliest CS-based guided reconstruction methods was proposed by Ehrhardt and Betcke (2016) introducing structure-guided total variation (STV), which assumes the sparse coefficients of the reconstruction to be partially known based on the edge features in the reference scan. Later work introduced adaptive elements into the multi-contrast CS framework, e.g. Weizman et al. (2016) proposed adaptive weighting-based guided CS and Song et al. (2020) used adaptive sparse domains based on coupled dictionary learning. In the latter, the problem was formulated using a patch-level linear model comprising coupled and distinct sparse dictionary representations of the two contrasts. This model resembles a content/style model in form, although it is more restrictive. A general drawback of classical methods compared to deep learning-based ones is their lower flexibility. End-to-end learning-based methods (Zhou and Zhou, 2020; Yang et al., 2020; Liu et al., 2021a,b; Feng et al., 2022; Lei et al., 2023), on the other hand, supply the reference scan as an additional input to a deep reconstruction model allowing it to automatically learn the suitable features to extract and transfer into the reconstruction, and have proven to be more effective than conventional algorithms. However, end-to-end methods require large paired training datasets comprising the ground-truth image and the k-space together with aligned reference images, which is too strong a constraint when working with retrospectively collected clinical data that reflects the natural inconsistencies of routine practice such as missing contrasts, differences in spatial resolutions, and the existence of inter-scan motion. Additionally, by relying on end-to-end-learned features, these methods are generally less interpretable than their conventional counterparts in that they do not explicitly model the multi-contrast problem in terms of the underlying shared and non-shared information. MC-VarNet (Lei et al., 2023) is an important exception, which uses a simple linear decomposition of the reference contrast into common and unique components, applying the common component for guidance.

A reconstruction method that is as effective as the learning-based methods while having more lenient data requirements and offering a high degree of interpretability is still needed. Our plug-and-play method relies on learning a deep non-linear content/style transform from image-domain data only, even if subject-wise paired images are not fully available.

2.2. Unpaired image-to-image modeling

Image-to-image modeling is the general problem of learning a mapping between two image domains and was first addressed by Pix2Pix (Isola et al., 2017) and CycleGAN (Zhu et al., 2017) in paired and unpaired settings, respectively. Another line of unpaired image translation methods, the first of which was UNIT (Liu et al., 2017), assumes a shared latent space underlying the two domains to explicitly represent shared information. However, both CycleGAN and UNIT assume a deterministic one-to-one mapping between the two domains, ignoring the fact that an image in one domain can have multiple valid renderings in the other. Deterministic image translation has been widely applied to MRI contrast-to-contrast synthesis (Dar et al., 2019; Oh et al., 2020; Yurt et al., 2021). However, fundamentally, these methods do not account for the variability of the scanning setup that influences the realized contrast level and the differential visibility of pathologies in the target image. Denck et al. (2021) partially address this problem by proposing contrast-aware MR image translation where the acquisition sequence parameters are fed into the network to control the output’s contrast level. However, this model is too restrictive since it assumes a single pre-defined mode

of variability (i.e. global contrast level) in the data, for which the labels (i.e. sequence parameters) must be available.

MUNIT (Huang et al., 2018) extended UNIT by modeling domain-specific variability in addition to domain-independent structure, enabling many-to-many mapping and thus overcoming the rigidity of UNIT. The result was a stochastic image translation model, which, given an input image, generates a distribution of synthetic images sharing the same "content" but differing in "style". More fundamentally, MUNIT is a learned invertible transformation between the image domains and the disentangled content/style domains. And unlike other content/style modeling frameworks such as (Kotovenko et al., 2019; Kwon and Ye, 2021; Wu et al., 2023), MUNIT models content and style as latent generative factors of the two image domains, providing precise distribution-level definitions for them. Clinical MR images of a given protocol contain multiple modes of variability, many of which are not known *a priori*. Compared to Denck et al. (2021), we make a broader assumption that the contrast-independent semantic information is local in nature and that the contrast-specific variations in the dataset can include global effects of acquisition settings as well as local anatomical features unique to the contrast. We model using an approach based on the MUNIT framework, referring to the shared and non-shared components as content and style, respectively.

2.3. Combining image translation with reconstruction

Acknowledging the limitation of MR cross-contrast prediction, some prior work has attempted combining it with multi-contrast reconstruction. A naive form of joint image synthesis and reconstruction, e.g. PROSIT (Mattern et al., 2020) and rsGAN (Dar et al., 2020), involves generating a synthetic image from the reference scan via deterministic image translation and using it in a classical L2-regularized least-squares reconstruction. More recent work by Xuan et al. (2022) proposed a joint image translation and reconstruction method which additionally accounts for misalignment between the reference and reconstructing images, with a follow-up work leveraging optimal transport theory (Wang et al., 2024). Levac et al. (2023) (whose approach we refer to as "PnP-Diffusion") formulate guided reconstruction as a highly general Bayesian maximum *a posteriori* estimation problem and solve it iteratively via Langevin update steps, using an image-domain diffusion model as the score function of the prior distribution. While these are promising directions, we propose an alternative approach that decomposes the multi-contrast problem in a more intuitive way – first, into two sub-problems, namely image modeling and image reconstruction; and second, within the image-domain model, the multi-contrast information is decomposed into content and style. This two-level decomposition results in a highly modular reconstruction algorithm with a built-in explanatory framework where (a) the guidance mechanism is a simple content-replacement operation, (b) the discrepancy between the supplied reference content and the true content of the target image represents a meaningful error term which can be minimized, and (c) the optimal content-encoding capacity of the model for a given two-contrast image dataset indicates the amount of shared structure that is available to be learned in this data and utilized in the reconstruction task.

3. Methods

3.1. Reconstruction problem

3.1.1. Undersampled MRI reconstruction

Given a set of P acquired k-space samples $y \in \mathbb{C}^P$ and the MRI forward operator $A \in \mathbb{C}^{P \times Q}$, CS reconstruction of the image $x \in \mathbb{C}^Q$ with Q voxels is given as

$$\min_x \|Ax - y\|_2^2 + \lambda \|\Psi x\|_1, \quad (1)$$

where Ψ is some sparsifying transform (e.g. wavelet) and λ is the regularization strength. A commonly used algorithm to solve this optimization problem is ISTA, which iteratively applies the following two update steps:

$$r^k \leftarrow \Psi^H \text{soft}(\Psi x^{k-1}; \lambda), \quad (2)$$

$$x^k \leftarrow r^k - \eta A^H (Ar^k - y). \quad (3)$$

Eq. (2) performs soft-thresholding in the transform domain, thereby reducing the incoherent undersampling artifacts in image x^{k-1} , whereas (3) enforces soft data consistency on image r^k by taking a single gradient descent step over the least-squares term, controlled by step size η .

3.1.2. Plug-and-play denoiser

Plug-and-play methods replace the analytical operation of (2) with off-the-shelf denoisers. A CNN-based denoiser is of special interest as it incorporates a learning-based component into iterative reconstruction. Given a CNN model f_θ trained to remove i.i.d. Gaussian noise from an image, PnP-CNN (Ahmad et al., 2020) modifies Eq. (2) to

$$z^k \leftarrow f_\theta(x^{k-1}). \quad (4)$$

3.1.3. Plug-and-play content consistency operator

In guided reconstruction, a spatially aligned reference x_1^{ref} is available, which captures the same underlying *semantic content* as the target reconstruction. Inspired by the PnP design, we cast the problem of incorporating prior information from x_1^{ref} into the reconstruction iterate x_2^{k-1} as enforcing a hard consistency between this image iterate and its semantic content estimated from the reference. We propose a *content consistency operator* $g_M(\cdot; c)$ such that

$$z_2^k \leftarrow g_M(x_2^{k-1}; c), \quad (5)$$

where a content/style model M decomposes x_2^{k-1} into content and style, followed by a replacement of this corrupted content with high-quality content c derived from x_1^{ref} and composing the improved image z_2^k from it. The model M is learned separately via an offline procedure and constitutes the core of our plug-and-play design. Before formally defining the operator $g_M(\cdot; c)$ and developing the reconstruction algorithm, we discuss in the following section the design and learning of the content/style model M .

3.2. Content/Style modeling

Given an image dataset of two MR contrasts, we make the general assumption that there exists an underlying contrast-independent structure which, influenced by arbitrary contrast-specific factors, is rendered as the contrast images. We formulate our content/style model based on the MUNIT framework (Huang et al., 2018).

3.2.1. Unpaired MUNIT pre-training

We define an image domain as the set \mathcal{X}_i of images of a certain contrast comprising the dataset, where $i \in \{1, 2\}$. "Content" $c \in \mathcal{C}$ is defined as the underlying contrast-independent structure and is represented as a set of feature maps, whereas "style" $s_i \in \mathcal{S}_i$ corresponds to the various modes of variability in one domain which cannot be explained by the other, e.g. global effects of acquisition settings, contrast-specific tissue features, etc., and is represented as a low-dimensional vector.

MUNIT posits the existence of functions $G_i^* : \mathcal{C} \times \mathcal{S}_i \rightarrow \mathcal{X}_i$ and their inverses $E_i^* = (G_i^*)^{-1}$, and learns them jointly via unpaired training, given samples from marginal distributions $p(x_i)$. In practice, the encoder E_i is split into content encoder E_i^c and style encoder E_i^s . Thus, the content/style model is specified as $M = \{E_1^c, E_2^c, E_1^s, E_2^s, G_1, G_2\}$.

The MUNIT loss function is comprised of four terms:

$$\mathcal{L}_{\text{MUNIT}} = \mathcal{L}_{\text{GAN}} + \alpha_1 \mathcal{L}_{\text{image}}^{\text{self}} + \alpha_2 \mathcal{L}_{\text{content}}^{\text{self}} + \alpha_3 \mathcal{L}_{\text{style}}^{\text{self}}, \quad (6)$$

where

$$\mathcal{L}_{\text{GAN}} = \mathbb{E}_{x_1 \sim p(x_1), s_2 \sim q(s_2)} [(1 - D_2(G_2(E_1^c(x_1), s_2)))^2] + \mathbb{E}_{x_2 \sim p(x_2), s_1 \sim q(s_1)} [(1 - D_1(G_1(E_2^c(x_2), s_1)))^2], \quad (7)$$

$$\mathcal{L}_{\text{image}}^{\text{self}} = \mathbb{E}_{x_1 \sim p(x_1)} [\|x_1 - G_1(E_1^c(x_1), E_1^s(x_1))\|_1] + \mathbb{E}_{x_2 \sim p(x_2)} [\|x_2 - G_2(E_2^c(x_2), E_2^s(x_2))\|_1], \quad (8)$$

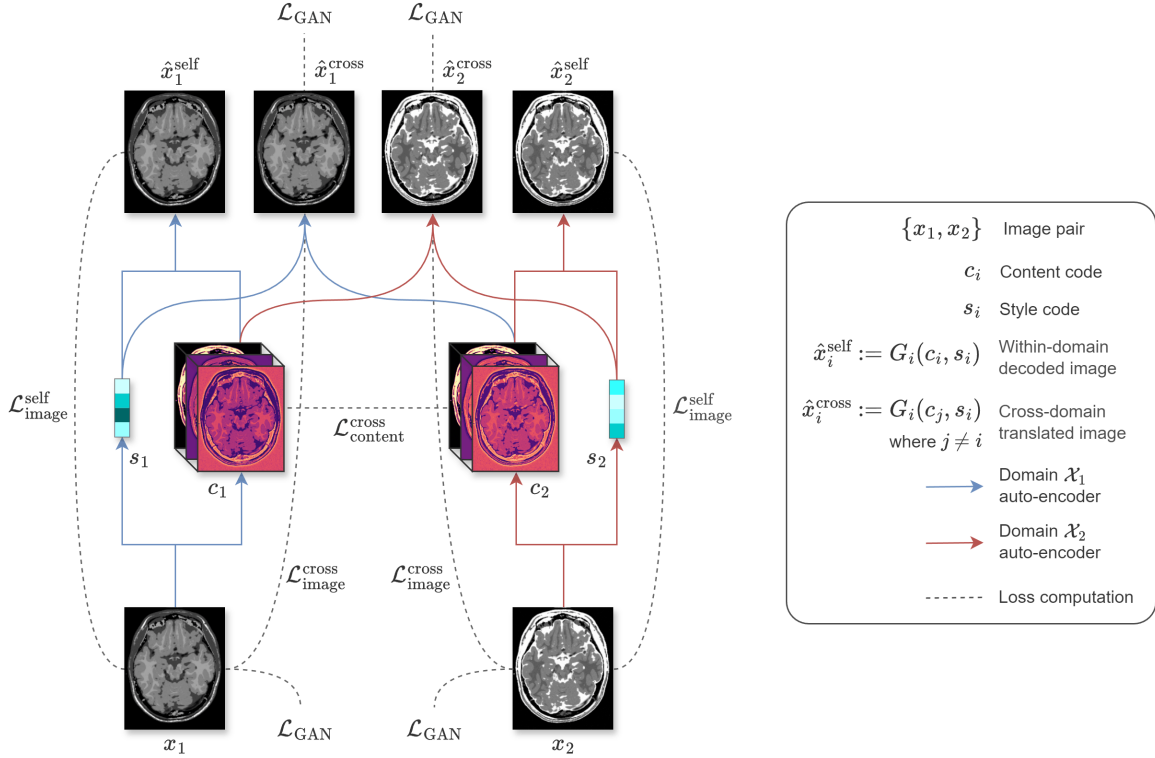


Figure 2: Our proposed paired fine-tuning (PFT) stage for improving the alignment of the content representations of the two domains given a small dataset of paired images.

$$\mathcal{L}_{\text{content}}^{\text{self}} = \mathbb{E}_{c_1 \sim p(c_1), s_2 \sim q(s_2)} [\|c_1 - E_2^c(G_2(c_1, s_2))\|_1] + \mathbb{E}_{c_2 \sim p(c_2), s_1 \sim q(s_1)} [\|c_2 - E_1^c(G_1(c_2, s_1))\|_1], \quad (9)$$

$$\mathcal{L}_{\text{style}}^{\text{self}} = \mathbb{E}_{c_1 \sim p(c_1), s_2 \sim q(s_2)} [\|s_2 - E_2^s(G_2(c_1, s_2))\|_1] + \mathbb{E}_{c_2 \sim p(c_2), s_1 \sim q(s_1)} [\|s_1 - E_1^s(G_1(c_2, s_1))\|_1]. \quad (10)$$

$\mathcal{L}_{\text{image}}^{\text{self}}$ is the image recovery loss, which promotes preservation of the image information in the latent space. $\mathcal{L}_{\text{content}}^{\text{self}}$ and $\mathcal{L}_{\text{style}}^{\text{self}}$ are the content and style recovery losses, respectively, which specialize parts of the latent code into content and style components. \mathcal{L}_{GAN} is the adversarial loss, which enables unpaired training by enforcing distribution-level similarity between synthetic and real images via discriminators D_1 and D_2 . α_1 , α_2 , and α_3 are hyperparameters. For our purpose, we consider the MUNIT training process as the pre-training stage of our content/style model.

3.2.2. Paired fine-tuning

While the pre-training stage learns useful content/style representations, we adapt the model to our task by improving its content preservation. To this end, we propose a paired fine-tuning (PFT) stage which more strongly aligns the content representations of the two domains given a modest amount of paired data. Given samples from the joint distribution $p(x_1, x_2)$, our fine-tuning objective is expressed as

$$\mathcal{L}_{\text{PFT}} = \mathcal{L}_{\text{GAN}} + \beta_1 \mathcal{L}_{\text{image}}^{\text{self}} + \beta_2 \mathcal{L}_{\text{image}}^{\text{cross}} + \beta_3 \mathcal{L}_{\text{content}}^{\text{cross}}, \quad (11)$$

where

$$\mathcal{L}_{\text{image}}^{\text{cross}} = \mathbb{E}_{\{x_1, x_2\} \sim p(x_1, x_2)} [\|x_2 - G_2(E_1^c(x_1), E_2^s(x_2))\|_1 + \|x_1 - G_1(E_2^c(x_2), E_1^s(x_1))\|_1], \quad (12)$$

$$\mathcal{L}_{\text{content}}^{\text{cross}} = \mathbb{E}_{\{x_1, x_2\} \sim p(x_1, x_2)} [\|E_1^c(x_1) - E_2^c(x_2)\|_1]. \quad (13)$$

$\mathcal{L}_{\text{image}}^{\text{cross}}$ is a pixel-wise image translation loss, which provides image-level supervision, and $\mathcal{L}_{\text{content}}^{\text{cross}}$ is a paired content loss, which penalizes discrepancy between the contents. β_1 , β_2 , and β_3 are an additional set of hyperparameters. Note that our PFT preserves the bi-directionality of the content/style model, a property which will later be essential for generalization over different reconstruction tasks.

3.2.3. Network architecture and content capacity

Following the original MUNIT paper (Huang et al., 2018), our content encoders E_i^c consist of an input convolutional layer potentially followed by strided downsampling convolutions, and finally a series of residual blocks. Style encoders E_i^s consist of input and downsampling convolutions followed by adaptive average pooling and a fully-connected layer that outputs the latent vector. Decoders G_i follow a similar structure as the content encoders except in reverse. Style is introduced into the decoder via AdaIN operations which modulate the activation maps derived from the content. We observe that in this architecture, the ratio between the content resolution and the image resolution reflects the level of local structure one expects to be shared between the two domains. This (relative) content resolution is thus an inductive bias built into the model, which we refer to as the model’s *content capacity* and define as

$$J_M := \frac{H_c W_c}{H_x W_x}, \quad (14)$$

where H_x and W_x are the height and width of the input image and H_c ($\leq H_x$) and W_c ($\leq W_x$) are those of the corresponding content maps. This ratio is controlled by changing the number of up/downsampling blocks in the networks. Our notion of content capacity is closely related to the more general concept of the locality bias of image-to-image models (Richardson and Weiss, 2021). A content/style model with a high content capacity has a large content resolution, allowing it to learn a rich, highly expressive content representation that strongly influences the output’s structure. Consequently, the model’s style spaces are restricted to learn mostly low-level global features. By finding the *optimal content capacity* for a given two-contrast image-domain dataset, one can quantify the amount of shared spatial information in this dataset, which will have consequences on the effectiveness of guidance in the reconstruction.

3.3. Iterative reconstruction based on content consistency

Given the content/style model M , we consider \mathcal{X}_1 and \mathcal{X}_2 as reference and target domains, respectively, in our guided reconstruction task, and define the content consistency operator $g_M(\cdot; c)$ from Eq. (5) as

$$x_2^{\text{cc}} = g_M(x_2^{\text{us}}; \hat{c}) := G_2(\hat{c}, E_2^s(x_2^{\text{us}})), \quad (15)$$

where x_2^{us} is the image containing undersampling artifacts, x_2^{cc} is the content-consistent image, and $\hat{c} = E_1^c(x_1^{\text{ref}})$ is the reference content. This operation improves x_2^{us} by simply replacing its aliased content with the content estimated from x_1^{ref} , a rule which will later be softened with (17).

Note that this is a radical operation as it discards all structure contained in x_2^{us} , retaining only a compact style code $\hat{s}_2 = E_2^s(x_2^{\text{us}})$. Let x_2^* be the ground truth reconstruction with content c^* and style s_2^* . The success of our content consistency operation depends on three conditions – (a) \hat{c} and c^* are rich, high-resolution representations of the underlying anatomy, (b) \hat{c} is close to c^* , and (c) \hat{s}_2 is close to s_2^* . The first condition is satisfied provided that there is sufficient amount of shared structure between the reference and target domains and that the model has high content capacity J_M for capturing a highly expressive content. The second condition is roughly satisfied, as seen in Fig. 3a, because the model is explicitly trained to minimize content error, but more on this later. On the other hand, it is not obvious that the third condition should hold too and it hence deserves a closer look. If the first condition is satisfied, the optimal model will have a high content capacity and consequently, style would represent mostly low-level global image features, e.g. contrast variations (see Section 3.2.3). This is observed in practice as shown in Fig. 3b. It is a well known fact that image contrast is contained prominently in the center of the k-space. Hence, the estimate \hat{s}_2 can be made arbitrarily close to s_2^* by sufficiently sampling the k-space center, as demonstrated empirically in Fig. 3c.

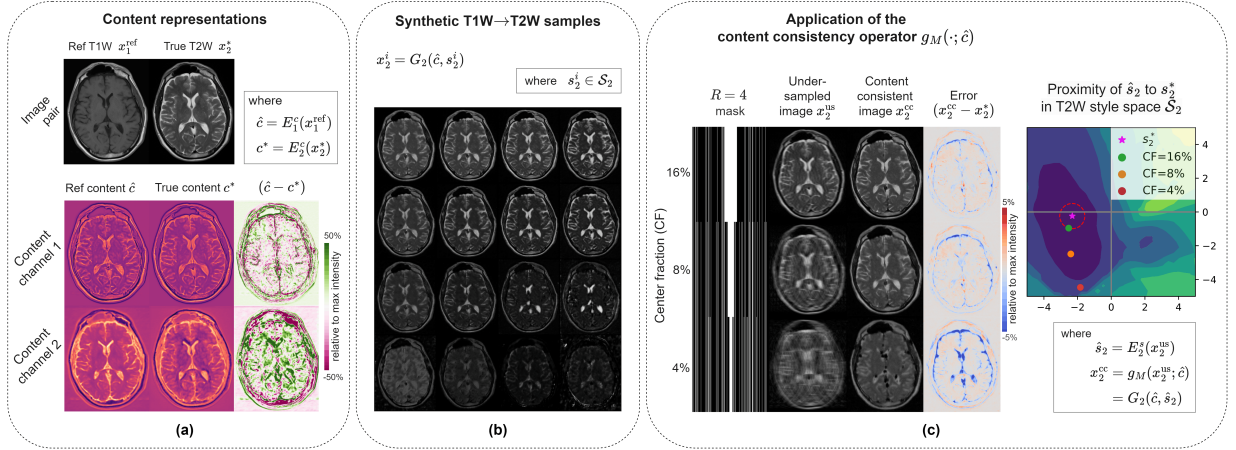


Figure 3: Demonstration of the content consistency operator $g_M(\cdot; c)$ based on a content/style model M . The image pair shown here are NYU fastMRI brain DICOMs, practical details regarding which are provided in Section 4. (a) A T1W/T2W image pair and the corresponding content maps showing that the two contents generally agree while there is also some discrepancy between them. (b) Synthetic T2W images generated from 16 style codes grid-sampled from \mathcal{S}_2 , showing that style encodes mostly the image contrast. (c) Ground truth T2W x_2^* is corrupted to x_2^{us} using $R=4$ undersampling with three different center fractions and the operator $g_M(\cdot; c)$ is applied to each case, showing that sampling more low-frequency lines leads to more accurate style estimate \hat{s}_2 and hence a better content-consistent image x_2^{cc} . Contours in \mathcal{S}_2 indicate the level set of MAE of the synthetic images corresponding to styles from those regions. The red circle indicates a style estimation NMSE of 0.1.

Applying data consistency update (3) following $g_M(\cdot; \hat{c})$ in repetition yields an ISTA-based iterative scheme. Here, our content consistency update complements the data consistency update in the sense that while the latter forces the image estimate to be consistent with the given (measured) k-space data y , the former forces it to be consistent with the given (prior) content \hat{c} .

Algorithm 1 PnP-CoSMo iterative guided reconstruction

Require: $y, A, x_1^{\text{ref}}, M, \eta, \gamma$ ▷ where $M = \{E_1^c, E_1^s, E_2^c, E_2^s, G_1, G_2\}$

- 1: $k \leftarrow 0$
- 2: $x_2^k \leftarrow A^H y$ ▷ Initialize reconstruction
- 3: $c^k \leftarrow E_1^c(x_1^{\text{ref}})$ ▷ Initialize content
- 4: **repeat**
- 5: $k \leftarrow k + 1$
- 6: $z_2^k \leftarrow g_M(x_2^{k-1}; c^{k-1})$ ▷ Content consistency update
- 7: $x_2^k \leftarrow z_2^k - \eta A^H (A z_2^k - y)$ ▷ Data consistency update
- 8: $c^k \leftarrow c^{k-1} - \gamma \nabla_c \|AG_2(c^{k-1}, E_2^s(x_2^k)) - y\|_2^2$ ▷ Content refinement (CR) update
- 9: **until** convergence
- 10: **return** x_2^k

The core assumption of an idealized content/style model is that contents \hat{c} and c^* are identical. However, in reality, this assumption will not hold, and a discrepancy between the two contents is to be expected. There are two possible sources of this discrepancy – (a) model-related, e.g. fundamental limits such as irreducible error¹ and practical issues like sub-optimal network design and training, and (b) reference image-related, e.g. presence of artifacts independent of the target reconstruction. We refer to this gap between \hat{c} and c^* as *content discrepancy*. Fig.3a shows content discrepancy as observed empirically. During reconstruction, the error in \hat{c} would limit the efficacy of the operator $g_M(\cdot; \hat{c})$, affecting the reconstruction quality. While

¹If perfectly zero error was possible, one could perfectly predict the (distribution of) target image from the reference without any measurement.

model-related discrepancy is partly tackled by PFT (Section 3.2.2), we now propose a *content refinement* (CR) process to correct for the remaining discrepancy in the reconstruction stage. Since we have no direct access to the true content c^* , but only to undersampled k-space measurements y , we aim at solving the following minimization sub-problem in CR

$$\min_c \|AG_2(c, \hat{s}_2) - y\|_2^2, \quad (16)$$

starting from the initial point $\hat{c} = E_1^c(x_1^{\text{ref}})$ and for a given style estimate \hat{s}_2 . The augmented forward operator $AG_2(\cdot)$ is a composition of the linear MRI forward operator A and the non-linear content/style decoder G_2 , and it maps the content domain to the k-space domain. The error between the predicted k-space $AG_2(c, \hat{s}_2)$ and the measured data y serves as a proxy for content discrepancy, which can be computed and minimized during the reconstruction. We approximate the solution with a single gradient descent step

$$c^k \leftarrow c^{k-1} - \gamma \nabla_c \|AG_2(c^{k-1}, \hat{s}_2^k) - y\|_2^2, \quad (17)$$

initialized as $c^0 \leftarrow E_1^c(x_1^{\text{ref}})$ and updated every k^{th} iteration with step size γ following the data consistency and content consistency updates. Hence, by aligning the content c with k-space data y and correcting the discrepancy, the CR module aligns content consistency updates with data consistency updates. With this additional component in place, we obtain our PnP-CoSMo reconstruction algorithm (Algorithm 1). Note that unlike content, the style of the image estimate need not be explicitly aligned with the k-space. Since the style information is assumed to be derived largely from the k-space data, the data consistency update applied on the image implicitly "corrects" its style. Thus, as the image converges, we hypothesize that style would converge as well.

4. Experimental setup

4.1. Experiment design

We conducted four sets of experiments to comprehensively evaluate PnP-CoSMo – (a) analyses on simulated MRI images, (b) benchmark against end-to-end methods on the public NYU fastMRI brain data (Knoll et al., 2020; Zbontar et al., 2018), (c) benchmark and ablation on clinical multi-coil raw data, and (d) a preliminary radiological evaluation. Without loss of generality, we considered the case of reconstructing T2W scans using T1W references and focused on head applications, except in the NYU benchmark where the reverse case of T2W-guided T1W reconstruction was considered as well.

4.1.1. Analyses on simulated MR data

The goal of our simulation experiments was to empirically test several properties of our algorithm under highly controlled settings. To this end, we used simulated T1W and T2W images based on BrainWeb phantoms (Collins et al., 1998). BrainWeb provides 20 anatomical models of normal brain, each comprised of fuzzy segmentation maps of 12 tissue types. The 20 volumes were first split into the model training (18), model validation (1), and reconstruction testing (1) subsets. 2D T1W and T2W spin-echo scans in the transversal plane were simulated using TE/TR values randomly sampled from realistic ranges, specifically $\text{TR} \in [300, 700]$ and $\text{TE} \in [5, 25]$ for T1W scans, and $\text{TR} \in [1800, 2200]$ and $\text{TE} \in [70, 120]$ for T2W scans. For testing the reconstruction, 2D single-coil T2W k-space data was simulated via Fourier transform and 1D Cartesian random sampling at various accelerations. We analyzed the effect of the content/style model’s disentanglement level and its content capacity on the reconstruction quality, the convergence of the PnP-CoSMo algorithm, and the effectiveness, robustness, and tuning of the CR module.

4.1.2. Benchmark on public NYU fastMRI DICOM data

In the NYU benchmark, we compared PnP-CoSMo against state-of-the-art reconstruction methods belonging to both end-to-end and plug-and-play paradigms. First, we sought to answer the following question – can PnP-CoSMo, which requires only image-domain training data, outperform end-to-end methods, which additionally require k-space training data and are optimized to directly solve the reconstruction problem?

Furthermore, end-to-end methods are task-specific models where the reference and target contrasts are fixed, e.g. T1W as reference and T2W as target. On the other hand, the content/style model used in PnP-CoSMo does not possess this kind of uni-directionality. Hence, we sought to assess the generalizability of PnP-CoSMo across two different reconstruction tasks: (a) T2W reconstruction with guidance from T1W reference and (b) T1W reconstruction with guidance from T2W reference. Finally, we compared PnP-CoSMo against other plug-and-play methods, which share a similar design pattern as ours where the modeling/learning problem is decoupled from the reconstruction problem and the requirement is only image-domain training data.

The public NYU fastMRI brain dataset includes multi-coil raw data and DICOM scans of 4 contrasts – T1W with and without gadolinium agent, T2W, and FLAIR. For multi-contrast experiments, however, the NYU raw dataset does not provide subject labels for pairing the contrasts. Therefore, instead of the NYU raw data, we used the NYU DICOMs in this study, following Xuan et al. (2022). A paired DICOM subset of 327 subjects was obtained based on T2W and non-gadolinium T1W scans, all of them being either 2D spin echo or turbo spin echo acquisitions in the transverse plane with median in-plane FOV of 220×220 mm² for both, in-plane voxel size of 0.69×0.69 mm² for T1W scans and 0.57×0.57 mm² for T2W scans, slice thickness of 5 mm for both, FA=20-150°, TR=220-874 ms, TE=2.46-17 ms, and ETL=1-5 for T1W scans, and FA=90-180°, TR=2696-8910 ms, TE=9.9-119 ms, and ETL=11-27 for T2W scans. All T1W scans were rigid-registered with the corresponding T2W scans. Single-coil k-space data was simulated via Fourier transform with 1D Cartesian random sampling at $R \in \{2, 3, 4, 5\}$ and added Gaussian noise of $\sigma = 0.01 \max(x_2^*)$.

The dataset was split into three folds at the subject-level for cross-validation based on random shuffling, with two partitions representing training data and one representing the test data in each fold. For PnP-CoSMo, all images from the training set were used to pre-train (ignoring the pairing information) and fine-tune (utilizing the pairing information) the content/style model, whereas the end-to-end methods were trained on paired examples composed of the reference image, the target contrast k-space, and its ground truth image. The plug-and-play baselines, were trained, like PnP-CoSMo, on the full image-domain data in the cross-validation training folds.

We benchmarked PnP-CoSMo against three end-to-end methods and three plug-and-play methods. Among the end-to-end baselines we included one well-known single-contrast network, namely MoDL (Aggarwal et al., 2018), and two recent multi-contrast networks, namely MTrans (Feng et al., 2022) and MC-VarNet (Lei et al., 2023). These networks were evaluated on the aforementioned two reconstruction tasks, assessing both their in-distribution and out-of-distribution performance. Specifically, for the T2W reconstruction task, "in-distribution" means that the end-to-end model was trained to reconstruct T2W images, whereas "out-of-distribution" means the model was trained to reconstruct T1W images but applied on the T2W reconstruction task, and *vice versa*. While MC-VarNet and MTrans used the reference image information, MoDL ignored the reference information. Among the plug-and-play baselines we included a single-contrast method, namely PnP-CNN (Ahmad et al., 2020), and two guided methods, namely PnP-Diffusion (Levac et al., 2023) and PROSIT (Mattern et al., 2020). Note that these methods, like PnP-CoSMo, are not contrast-task-specific in the same way end-to-end models are, and thus the concept of in-distribution and out-of-distribution tasks does not apply to them.

4.1.3. Benchmark and ablation on in-house LUMC multi-coil datasets

In our benchmark on clinical multi-coil data, the goal was to test PnP-CoSMo on a constrained real-world problem where only the image-domain data was available for training. This is often the case, as in clinical practice raw data is discarded after acquisition and only the final reconstructions are retained. Moreover, T1W/T2W images are often not fully subject-wise paired, e.g. due to missing acquisitions, representing a realistic case of data imbalance.

Our in-house data consisted of brain scans of patients from LUMC, the use of which was approved for research purpose by the institutional review board. A total of 1669 brain scans were obtained from 817 clinical MR examinations of 630 patients acquired on 3T Philips Ingenia scanners. We focused on accelerating two T2W sequences – (a) 2D T2W TSE transversal and (b) 2D T2W TSE coronal. For guidance, two corresponding T1W sequences were used – (a) 3D T1W TFE transversal and (b) 3D T1W

Table 1: Overview of the sequences in the LUMC datasets.

Sequence Params	LUMC-TRA			LUMC-COR		
	3D T1W TFE	2D T2W TSE	3D T1W TSE	2D T2W TSE		
FA (deg)	8	90	80-90	90		
TR (ms)	9.8-9.9	4000-5000	500-800	2000-3500		
TE (ms)	4.6	80-100	6.5-16	90-100		
ETL	200	14-18	10-13	17-19		
Voxel size (mm)	0.98×0.99 ×0.91	0.4×0.54	0.59×0.62 ×1.19	0.39×0.47		
Slice thick. (mm)	–	3	–	2		
FOV (mm)	238×191 ×218	238×190	130×238 ×38	130×197		
Num slices	–	50	–	15		

Table 2: LUMC data split. The splits were made at the subject-level, i.e. each subject belonged to exactly one subset. Splits containing *only* image-domain data, specifically *image-train* and *image-val*, are marked with ³. Thus, the training of only image-domain models is feasible, thereby representing a real-world problem where end-to-end methods are not feasible. The *recon-val* and *recon-test* splits additionally include the raw T2W multi-coil k-space and coil sensitivities, which were used for tuning and evaluating the reconstruction algorithms. All of these data samples were used in the experiment.

Dataset	Split	Subjects	Sessions	Scans (T1W / T2W)
LUMC-TRA	<i>image-train</i> ³	295	418	360 / 415
	<i>image-val</i> ³	16	17	17 / 17
	<i>recon-val</i>	18	21	21 / 21
	<i>recon-test</i>	20	31	31 / 31
	Total	339	487	429 / 484
LUMC-COR	<i>image-train</i> ³	242	277	269 / 272
	<i>image-val</i> ³	18	18	18 / 18
	<i>recon-val</i>	15	18	18 / 18
	<i>recon-test</i>	16	17	17 / 17
	Total	291	330	322 / 325

TSE coronal. The transversal and coronal protocols were considered as two separate datasets, namely LUMC-TRA and LUMC-COR. Table 1 shows an overview of the four sequences. Note that the in-plane resolution of the T1W scans was 1.3-2.5 times as low as that of the T2W scans, making these datasets more challenging for T1W-guided T2W reconstruction.

Each of the two LUMC datasets was split into *image-train*, *image-val*, *recon-val*, and *recon-test*. The former two splits contained only image-domain data, which was used to train and validate the content/style models. The models were pre-trained on the full *image-train* splits, ignoring any pairing between T1W and T2W scans. Additionally, 20 subjects from the *image-train* split were designated for PFT where the pairing information was used in training and the reference scans were aligned via registration. The *recon-val* and *recon-test* splits additionally included multi-coil T2W raw data, which comprised 6-channel (LUMC-TRA) and 13-channel (LUMC-COR) k-space and coil sensitivity maps. This k-space was already undersampled (1D Cartesian random) at acquisition with clinical acceleration of $R=1.8-2$. We further undersampled it retrospectively to higher accelerations $R \in \{4, 6, 8, 10\}$ by dropping subsets of the acquired lines. The *recon-val* split was used to tune the reconstruction algorithm hyperparameters (such as CR step size γ for PnP-CoSMo, regularization weights for classical baselines, etc.), whereas *recon-test* was the held-out data on which the final metrics are reported. An overview of the data split is shown in Table 2. Spatially aligned images required by all but the unpaired training set were obtained via rigid registration and the reference T1W images were resampled to the T2W resolution. During unpaired training, all images were resampled to the median T2W resolution.

Given the absence of k-space training data, end-to-end reconstruction methods were not feasible as baselines. Hence, we compared PnP-CoSMo with only the feasible types of baselines, i.e. classical, semi-classical, and plug-and-play reconstruction and image-to-image translation. Among classical methods, we used the unguided L1-wavelet CS (CS-WT) and the guided STV-based CS (CS-STV) (Ehrhardt and Betcke, 2016). As an unguided plug-and-play baseline, we used PnP-CNN (Ahmad et al., 2020), and as a representative image translation baseline, we compared against MUNIT itself. Using MUNIT, deterministic image translation was approximated by combining the reference content with 200 randomly sampled T2W style codes and taking a pixel-wise mean of the resulting synthetic images to obtain a single synthetic image. As semi-classical guided baseline, we used PROSIT (Mattern et al., 2020), which combines deterministic image translation with L2-regularized least-squares reconstruction. Additionally, as an ablation study for PnP-CoSMo, we ablated PFT and CR to assess their contribution, and finally, as an upperbound for PnP-CoSMo representing zero content discrepancy, we disabled PFT and CR and used the ideal content c^* . In both NYU and LUMC benchmarks, we used three perceptual metrics for evaluation – SSIM, HaarPSI, and DISTS. While SSIM is used commonly, HaarPSI and DISTS are known to correlate better with visual judgment of image quality (Kastriulin et al., 2023). All three metrics are bounded in $[0, 1]$ where 1 represents perfect image quality. We conducted paired Wilcoxon signed-rank tests to measure statistical significance when comparing pairs of algorithms.

4.1.4. Preliminary radiological evaluation

Finally, as a supplement to the LUMC benchmark, we conducted a preliminary radiological evaluation with the goal of assessing the quality of PnP-CoSMo reconstructions in a concrete clinical context. The study was conducted on a small sample of the LUMC-TRA *recon-test* set. First, all 20 subjects from this set (see Table 2) were screened by a junior radiologist, for the presence of brain metastases, resulting in three scans included in this part of the study. The scoring was then performed independently by two senior neuroradiologists. The scoring system comprised two sets of criteria, namely visual quality and pathology. Four visual quality criteria were used, namely sharpness, noise, artifacts, and tissue contrast between gray and white matter and CSF. For pathology, we used three criteria, namely the number and sharpness of hyperintense areas within or surrounding metastases and the overall diagnostic quality of the scan for brain metastases. The images were scored using a five-point Likert scale (Mason et al., 2019) – (1) non-diagnostic, (2) poor, (3) fair, (4) good, and (5) excellent diagnostic quality.

Furthermore, we used PnP-CNN as a non-guided plug-and-play reconstruction baseline. We evaluated the two methods at four clinically realistic accelerations of $R \in \{3, 4, 5, 6\}$, which are close to the routine clinical acceleration of $R=2$ for this sequence. In total, nine images per patient, including the $(2 \times 4 = 8)$ reconstructions and the clinical ground truth (acquired at $R=2$ and reconstructed by the vendor software), were presented to the two observers who scored each image individually, blinded to the reconstruction method and R . The scores were then processed as follows. Given a reconstruction method and R , the scores for each Likert-scale criterion were expressed as an aggregate by computing the mean across the three subjects and the two observers. The number of visible metastases was expressed as the fraction of total metastases across the three subjects. Moreover, the agreement between the two observers was measured using Spearman’s rank correlation coefficient, computed separately on the Likert-scale scores and the metastasis count.

4.2. Implementation details

We used a similar general residual architecture for content/style encoders and decoders as in the original MUNIT paper (Xuan et al., 2022), except with an additional layer at the end of the content encoder to produce content maps of the specified number of channels. We used 2 or 4 content channels, depending on the content downsampling factor. The discriminators were implemented as multi-scale PatchGAN networks enabling them to locally assess the input images for realism at different scales. We used 1 scale in the BrainWeb simulations and three scales in the NYU and LUMC benchmark. We additionally conditioned the discriminators on foreground masks of the images to penalize background signal, and we used spectral normalization (Miyato et al., 2018) to stabilize the GAN training. For hyperparameters, we found that pre-training loss weight values $\alpha_1 = \alpha_2 = \alpha_3 = 1$ and paired fine-tuning values $\beta_1 = \beta_2 = \beta_3 = 1$ worked

generally well for the *in vivo* NYU and LUMC datasets. Of all these hyperparameters, α_2 and α_3 , which control the disentanglement level, are most interesting. Therefore, the tuning of α_2 and α_3 for the synthetic BrainWeb data is presented later in Section 5.1.1, where the optimal value was found to be $\alpha_2 = \alpha_3 = 0.1$ on this dataset. In the benchmarks, the step size γ of the CR module of PnP-CoSMo was tuned per acceleration for each dataset and the number of iterations was set to 200.

In the simulations, all content/style models were pre-trained for 200k and were not fine-tuned for the sake of simplicity, unless stated otherwise in Section 5.1. In both NYU and LUMC benchmarks, the content/style models were pre-trained for 400k iterations and fine-tuned for 50k iterations. We empirically found that a content/style model with content capacity $J_M=1$ was optimal for the NYU dataset, whereas models with capacity $J_M=1/4$ were optimal for the LUMC datasets. For the synthetic BrainWeb data, the effect of this parameter on the reconstructions is presented later in Section 5.1.2, where the optimal value was found to be $J_M=1$ when both contrasts have equal spatial resolution.

All software was implemented in PyTorch, and image registration was performed using Elastix (Klein et al., 2009). All training runs were performed on a compute node with an NVIDIA Quadro RTX 6000 GPU.

5. Results

In the following sections we report the results of our extensive evaluation. In Section 5.1, we report our analyses on the synthetic BrainWeb dataset. These include a sensitivity analysis with respect to the level of disentanglement of content and style (Section 5.1.1), content capacity analysis exposing the relation between reference image resolution and the reconstruction quality (Section 5.1.2), convergence analysis of our iterative algorithm (Section 5.1.3), and a series of analyses on the CR component including evaluating its effectiveness in correcting for contrast-specific structure small misalignments and the influence of the CR step size γ (Section 5.1.4). In Section 5.2, we present the results of our benchmark against three end-to-end and three plug-and-play baselines on the public NYU fastMRI data. In Section 5.3, results of our benchmark on our in-house LUMC multi-coil raw data are reported. Given the real-world constraints of our clinical datasets, specifically a collection of partially-paired image-domain training data and complete lack of k-space training data, PnP-CoSMo is compared with classical unguided and guided reconstruction algorithms, plug-and-play unguided and guided methods, and image-to-image translation. Furthermore, our ablation study of PnP-CoSMo on these datasets demonstrates the contribution of the PFT and CR components of PnP-CoSMo. Finally, in Section 5.4, results of our small preliminary radiological evaluation are reported.

5.1. Analyses on simulated MR data

5.1.1. Perturbation of disentanglement strength

PnP-CoSMo assumes that the content and style aspects of the images are sufficiently disentangled. Here, we evaluated the effect of perturbing the disentanglement loss weights α_2 and α_3 (Eq. (6)) of MUNIT on the PnP-CoSMo reconstruction quality. Table 3 shows the reconstruction PSNR for different weight values. We observed that optimal disentanglement, and thus the best reconstruction, was achieved at $\alpha_2 = \alpha_3 = 0.1$. At lower values, poor disentanglement of content and style in the model resulted in poor PnP-CoSMo reconstruction quality. This was expected since PnP-CoSMo relies on the assumption that the content representation is (sufficiently) contrast-independent, which was less enforced at these levels. At higher values, the training over-emphasized disentanglement while under-emphasizing the GAN and image recovery loss terms, thereby leading to worse preservation of image information in the latent space and thus, to worse reconstructions.

5.1.2. Content capacity analysis

PnP-CoSMo relies on a reference image of sufficiently high resolution to provide guidance to the reconstruction. The goal of this experiment was to determine the effect of lowering the reference image resolution on the reconstruction quality and using the content/style model’s content capacity (Eq. (14)) to explain this effect. We simulated 4 datasets, denoted as RefRes-1/ n , where $n \in \{1, 2, 4, 8\}$ represents the reference

Table 3: Reconstruction PSNR (dB) over the BrainWeb test volume (300 slices). PSNR worse than the conventional L1-wavelet CS reconstruction is marked as \dagger . A lower disentanglement strength results in insufficient poor separation of content from style, violating the modeling assumptions and resulting in worse reconstructions. Whereas, excessive focus on disentanglement sacrifices preservation of image information in the latent space, leading to highly lossy encoding and decoding in the model and, hence, to worse reconstructions.

Disentanglement Strength	R=2	R=4
$\alpha_2 = \alpha_3 = 10$	$15.14 \pm 0.06^\dagger$	$12.84 \pm 0.05^\dagger$
$\alpha_2 = \alpha_3 = 1$	28.43 ± 0.07	26.13 ± 0.07
$\alpha_2 = \alpha_3 = 0.1$	29.84 ± 0.05	27.33 ± 0.05
$\alpha_2 = \alpha_3 = 0.01$	25.34 ± 0.06	23.03 ± 0.05
$\alpha_2 = \alpha_3 = 0.001$	$18.17 \pm 0.07^\dagger$	$15.88 \pm 0.05^\dagger$

Table 4: Reconstruction PSNR (dB) over the BrainWeb test volume (300 slices) at $R=4$. Optimal content capacity J_M for each column (i.e. reference image resolution) corresponds to the best PSNR, shown in bold. PSNR worse than the conventional L1-wavelet CS reconstruction is marked as \dagger . Decrease in reference resolution results in a decrease in reconstruction quality. This is explained by a decreased amount of shared spatial information in the dataset as quantified by the optimal content capacity.

Model Config	Data Config			
	RefRes-1	RefRes-1/2	RefRes-1/4	RefRes-1/8
$J_M=1$	27.90 ± 0.08	21.17 ± 0.05	19.11 ± 0.07	$16.43 \pm 0.07^\dagger$
$J_M=(1/2)^2$	26.19 ± 0.08	22.80 ± 0.08	20.05 ± 0.08	$16.57 \pm 0.08^\dagger$
$J_M=(1/4)^2$	23.98 ± 0.08	20.88 ± 0.10	19.44 ± 0.09	16.88 ± 0.06

domain downsampling factor. In the $n=1$ case, the T1W/T2W images had the same resolution (as that of the underlying tissue maps), whereas in the subsequent cases, T1W images were blurred to contain only the lower $1/n$ frequency components, while maintaining the same spatial resolution. For each dataset, we trained three content/style models with content capacity $J_M=(1/m)^2$, where $m \in \{1, 2, 4\}$ is the content downsampling factor, which depends on the number of up/downsampling blocks in the networks. E.g. the $J_M=(1/2)^2$ model produced content maps half the spatial resolution of the $J_M=1$ model.

Table 4 compares PnP-CoSMo reconstruction quality across these configurations. PFT and CR were disabled here for simplicity. We observe two trends. First, the reconstruction quality generally decreases from left to right, eventually dropping below the conventional L1-wavelet CS reconstruction, suggesting a decrease in the amount of shared local information contained in the reference contrast. Second, the *optimal content capacity* of the model decreases with the reference resolution in accordance with the actual amount of this shared information. In other words, this optimal content capacity corresponds to the amount of contrast-independent structure the model discovers in the dataset, e.g. RefRes-1 dataset had 4 times as much shared structure (due to twice as large optimal content resolution) as RefRes-1/2 and RefRes-1/4 datasets and hence, the RefRes-1 dataset was significantly more effective in guided reconstruction. On the other hand, RefRes-1/2 and RefRes-1/4 datasets had similar levels of shared structure (i.e. $J_M=1/2^2=1/4$ times the full-resolution case) despite the lower reference resolution in RefRes-1/4, suggesting a more complex relationship between the reference resolution and the shared content. In the RefRes-1/8 case, PnP-CoSMo dropped to a similar level of quality as conventional CS, suggesting a lowerbound on the amount of shared information for PnP-CoSMo to be effective, specifically $J_M=1/4^2=1/16$ times the local information of the full-resolution case.

5.1.3. Convergence analysis

We explored the convergence of PnP-CoSMo by comparing it with two variants. The first used true content c^* of the ground truth T2W image, thus assuming zero content discrepancy and representing an upperbound of PnP-CoSMo. The second used reference content \hat{c} with CR module disabled, representing a lowerbound of PnP-CoSMo where the non-zero content discrepancy is not corrected. Here and in the following simulation experiments, we used the RefRes-1 dataset and the $J_M=1$ model, which was additionally fine-tuned on 2 training volumes for 50k iterations. Fig. 4 shows the convergence curves and intermediate reconstructions.

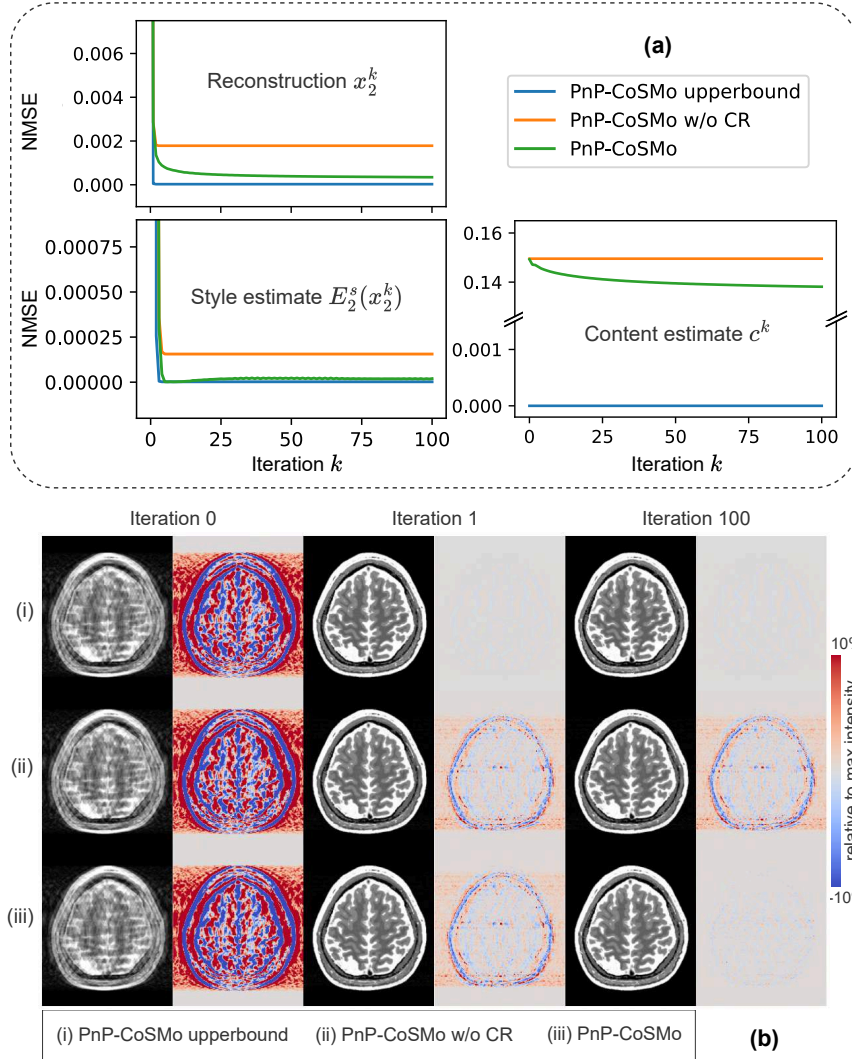


Figure 4: Convergence analysis on synthetic BrainWeb data. (a) Convergence curves for PnP-CoSMo and its two variants at $R=2$. (b) Evolution of the reconstruction shown with the corresponding error maps. In PnP-CoSMo with CR disabled and its upperbound version, i.e. both cases where the content stays constant, the style converges in a single iteration and so does the reconstruction. However, there is a notable discrepancy in the reference content which is reflected in the reconstruction error when CR is disabled. Enabling CR leads to an iterative correction of the content discrepancy, leading in turn to the reconstruction approaching the upperbound quality.

The upperbound version, given c^* , converged in a single iteration, while with \hat{c} , the ablated version converged equally fast but to a sub-optimal solution. Enabling the CR module closed the gap with the upperbound, although at the cost of slower convergence. It is also observed that the content discrepancy reduced when using CR and that the style estimate always converged within the first few iterations, as we hypothesized in Section 3.3.

5.1.4. Analyses on the content refinement procedure

The CR update step (Eq. 17) corrects of arbitrary discrepancies between the prior content and the measured k-space. We tested its robustness against two specific discrepancies: (a) contrast-specific structure (for e.g. a lesion) present in the target contrast but not in the reference contrast and (b) spatial misalignment in the reference contrast image. Additionally, the influence of the CR step size γ was also analyzed.

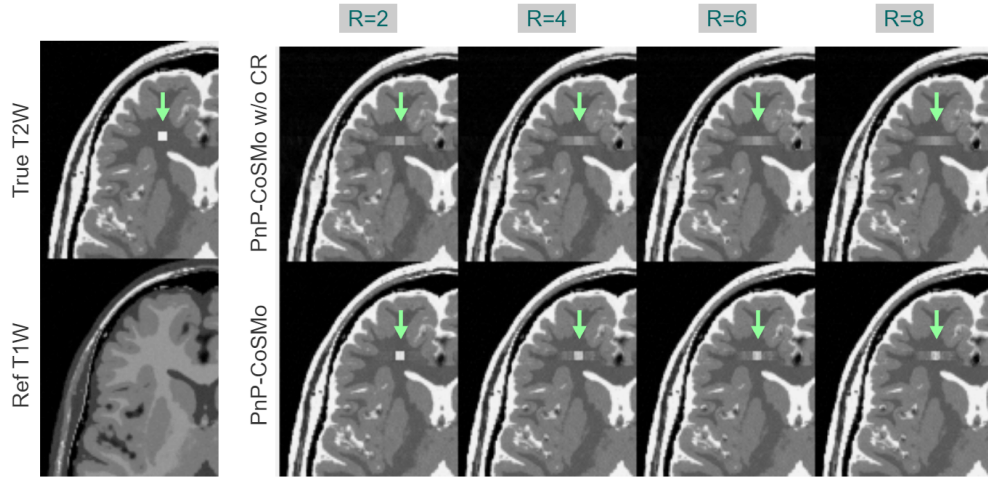


Figure 5: Lesion analysis on synthetic BrainWeb data. Given a contrast-specific structure in the T2W data such as the simulated lesion here which is absent in the reference image, our CR module contributes substantially in resolving it.

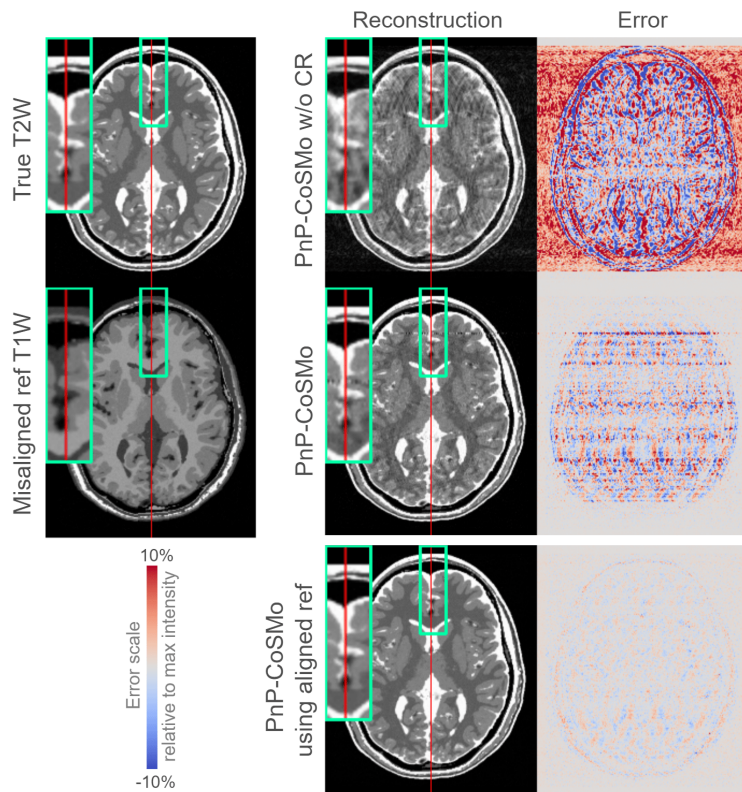


Figure 6: Misalignment analysis on synthetic BrainWeb data. A misaligned reference image (with 2° rotation) severely affected the reconstruction when CR was disabled, where enabling CR improved the robustness of the reconstruction process. A PnP-CoSMo reconstruction using an aligned reference is shown for comparison.

In order to test the effectiveness of the CR module in resolving structure present in the target contrast but absent in the reference contrast, we simulated a lesion in the T2W image and performed reconstruction with and without the CR module. As shown in Fig. 5, the CR module was able to recover the lesion fully

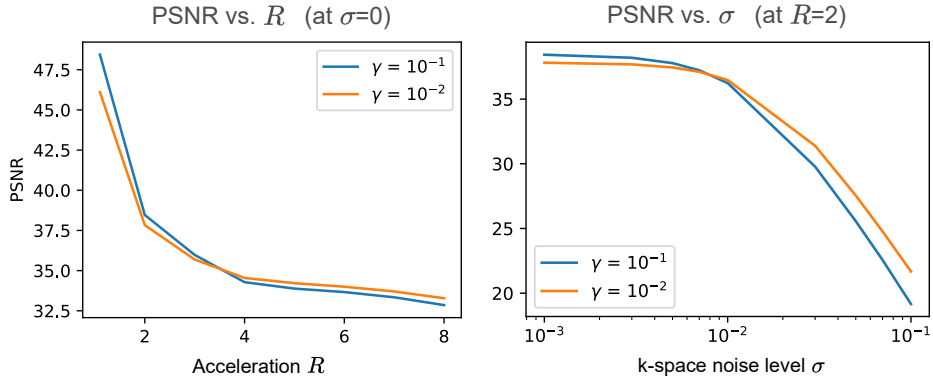


Figure 7: Sensitivity analysis for the CR step size γ on synthetic BrainWeb data. Reconstruction PSNR as a function of acceleration R and k-space noise level σ for different values of γ . With a decrease in quantity (via acceleration) and in quality (via noise) of the k-space data, the added value of CR drops as indicated by a lower optimal γ .

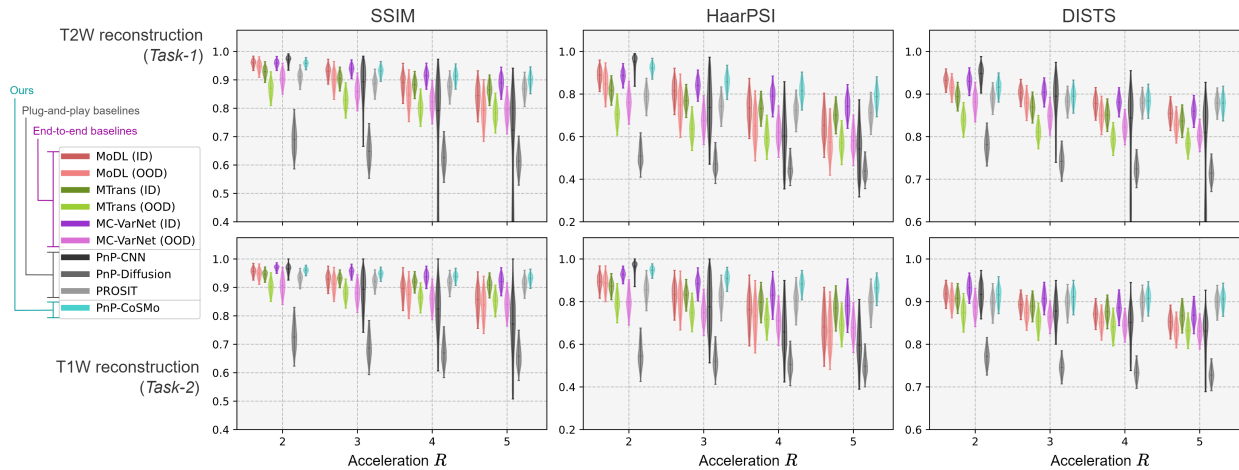


Figure 8: Evaluation plots from the cross-validation on the NYU DICOM dataset for the two reconstruction tasks. ID and OOD refer to in-distribution and out-of-distribution models, respectively. Note that while MTrans, MC-VarNet, PnP-Diffusion, and PROSIT are guided methods, MoDL and PnP-CNN are unguided methods and, hence, did not use the reference image information. In each individual task, our PnP-CoSMo showed competitive metrics compared to end-to-end methods and outperformed the other plug-and-play methods. Moreover, unlike the end-to-end methods, which require task-specific k-space training data and which drop in performance on the OOD task, PnP-CoSMo, by design, requires only a single content/style model for both tasks demonstrating its superior cross-contrast generalizability.

at $R=2$ and substantially at $R \in \{4, 6, 8\}$.

While PnP-CoSMo expects an aligned reference image at reconstruction time, the CR module should, in principle, correct for small misalignments. To test this, we simulated a 2° rotation in the reference image and performed reconstruction at $R=2$ with and without the CR module, comparing also with PnP-CoSMo that used an aligned reference image. As shown in Fig. 6, although the reconstruction was sensitive to the misalignment in the absence of CR, it significantly improved with CR enabled.

Finally, we also analyze the influence of the hyperparameter γ in Algorithm 1, which controls the CR step size. Fig. 7 shows reconstruction quality as a function of acceleration and k-space noise level, where we observe that the optimal γ decreased with the amount and quality of k-space data. This was expected as enforcing agreement with the k-space gradually becomes less beneficial, thereby contributing less to reconstruction quality.

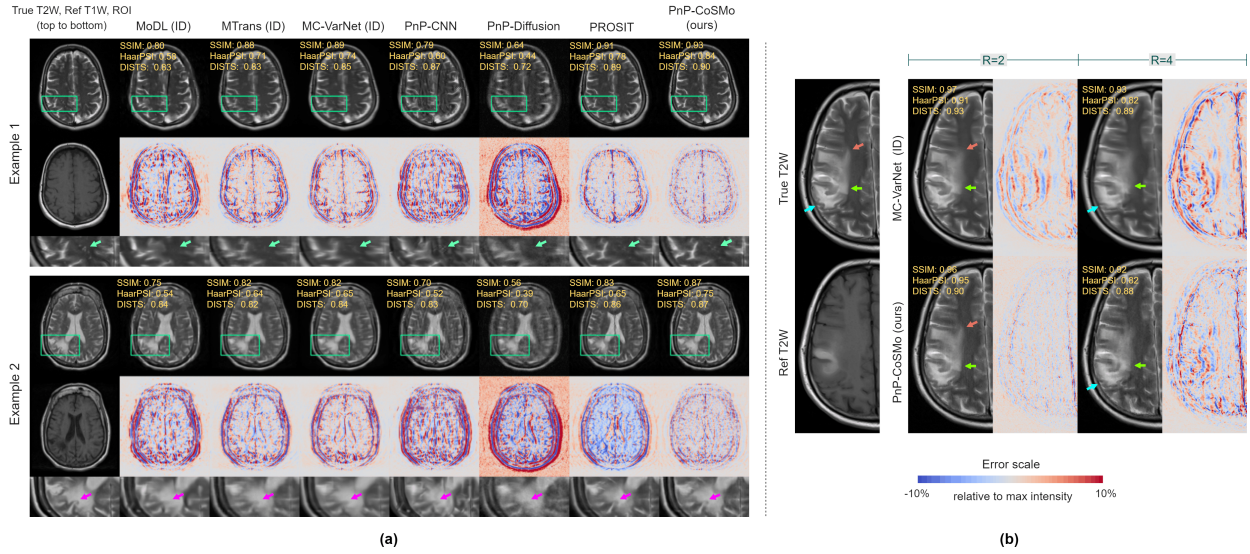


Figure 9: Examples from the NYU benchmark for our Task-1 (i.e. T2W reconstruction). (a) Comparison of PnP-CoSMo with the in-distribution end-to-end models and the plug-and-play baselines at the highest acceleration of $R=5$. PnP-CoSMo produced less blurring and resolved some of the finest details (green and magenta arrows). (b) Comparison between PnP-CoSMo and MC-VarNet at $R=2$ and $R=4$ on a pathological case where many features of the edema are T2W contrast-specific. Again, we observe sharper reconstructions with PnP-CoSMo compared to the end-to-end MC-VarNet, despite often slightly lower metrics.

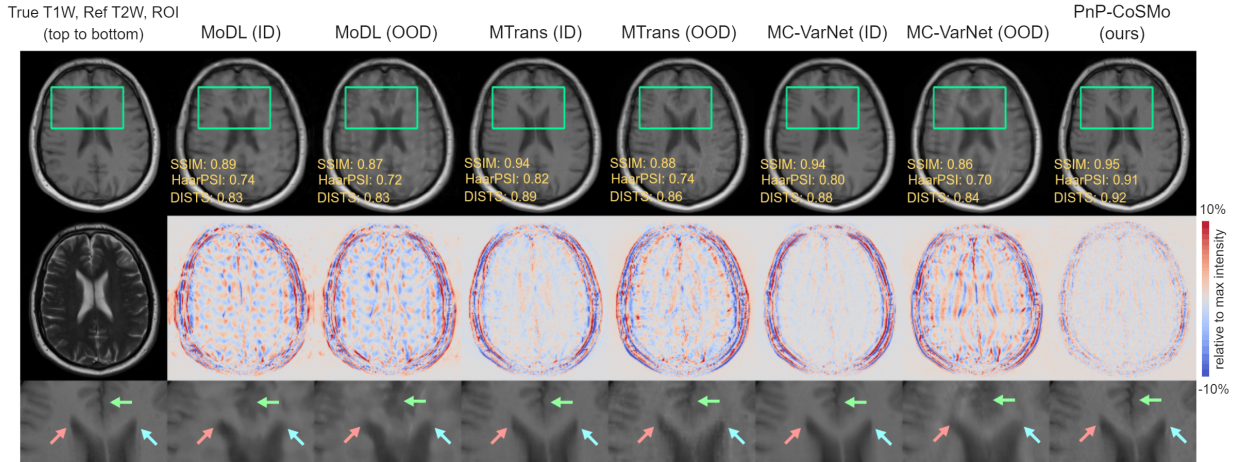


Figure 10: A test example from the NYU benchmark for our Task-2 (i.e. T1W reconstruction) at the highest acceleration of $R=5$ showing the cross-contrast generalizability of PnP-CoSMo. The in-distribution (ID) models were trained to solve Task-2 and subsequently applied on Task-2, whereas the out-of-distribution (OOD) ones were trained to solve Task-1 (i.e. T2W reconstruction) and subsequently applied on Task-2. All three end-to-end methods dropped in performance on the OOD case. PnP-CoSMo is immune to such a distribution shift by design. Moreover, it produced sharper reconstructions compared to the end-to-end models even in the ID case.

5.2. Benchmark on public NYU fastMRI DICOM data

In the NYU benchmarking setup considered here, let the T2W reconstruction task be denoted as Task-1 and the T1W reconstruction task as Task-2. In Task-1, guided methods use the corresponding T1W image as reference, and in Task-2, the T2W images are used as reference. Unguided methods such as MoDL and PnP-CNN ignore this side-information. Fig. 8 shows evaluation metrics for PnP-CoSMo and the end-to-end baselines on these two guided reconstruction tasks.

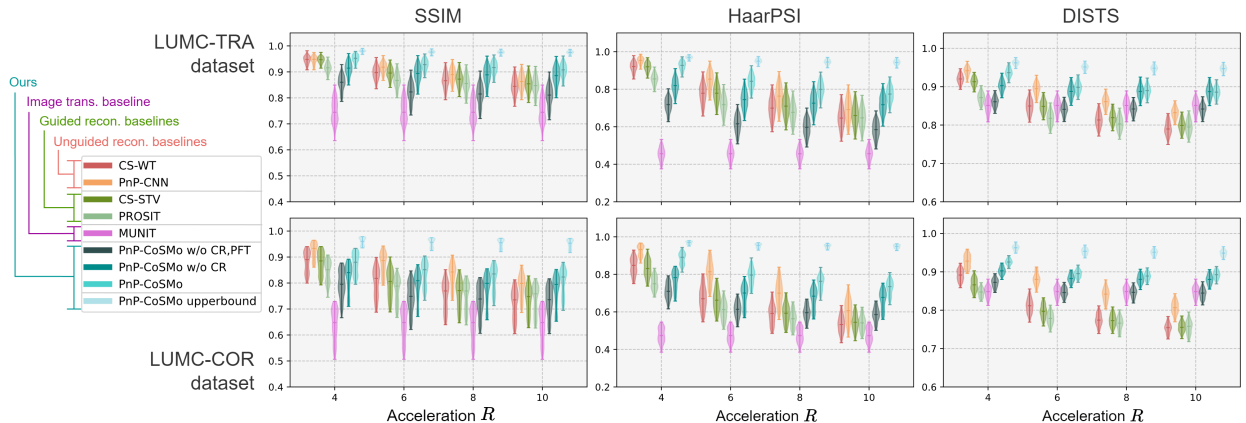


Figure 11: Evaluation plots over the *recon-test* subset of LUMC-TRA and LUMC-COR datasets consisting of 1366 and 200 slices, respectively. Compared to the unguided reconstruction baselines (CS-WT, PnP-CNN), PnP-CoSMo generally produced higher-quality images, especially at the higher accelerations, showing the added value of guidance at these accelerations. Compared to the guided reconstruction baselines (CS-STV, PROSIT), PnP-CoSMo was consistently better, demonstrating its more effective use of the reference information. PnP-CoSMo outperformed pure image translation (MUNIT), showing the value of incorporating k-space measurements. Finally, ablating the PFT and CR components from PnP-CoSMo consistently reduced the image quality, thus demonstrating their contribution. The PnP-CoSMo upperbound shows the theoretically achievable quality if the true content could be perfectly estimated.

We observe three main trends. First, comparing with the in-distribution reconstruction quality of the end-to-end baselines, PnP-CoSMo largely outperformed MoDL ($p < 0.05$ throughout, except for SSIM at $R=2$ and DISTS at $R \in \{2, 3\}$ on Task-1, and DISTS at $R=2$ on Task-2) and MTrans ($p < 0.05$ throughout), and was roughly comparable to MC-VarNet (e.g. with $p < 0.05$ on Task-2 in terms of DISTS at $R=3$ and SSIM at $R=4$) while often outperforming it ($p < 0.05$ throughout, except SSIM at $R \in \{2, 3, 4\}$ and DISTS at $R \in \{2, 3\}$ on Task-1, and SSIM at $R \in \{2, 3\}$ and DISTS at $R=2$ on Task-2). Compared to the plug-and-play baselines, PnP-CoSMo largely outperformed PnP-CNN ($p < 0.05$ throughout, except at $R=2$) and was significantly superior to PnP-Diffusion and PROSIT ($p < 0.05$ throughout for both). As shown in Fig. 9a, PnP-CoSMo could resolve certain fine details even at the highest acceleration of $R=5$, which both end-to-end and plug-and-play baselines fell short at. In the pathological case shown in Fig. 9b, PnP-CoSMo produced sharper reconstructions while preserving the structure of the edema better than (the in-distribution) MC-VarNet, despite slightly lower metrics, when many features of the edema were absent in the reference image.

Second, considering out-of-distribution generalization, the end-to-end methods consistently dropped in performance on the out-of-distribution tasks ($p < 0.05$ for all three models on both tasks at all 4 accelerations). This was expected since end-to-end models are explicitly trained to optimize for a given contrast task and will inevitably not generalize well across contrasts.

Third, PnP-CoSMo definitively outperformed the out-of-distribution variants of all the end-to-end models ($p < 0.05$ throughout). Since PnP-CoSMo does not depend on any task-specific k-space training data owing to both its plug-and-play design and because of the bi-directionality of the content/style model it uses, it is not susceptible to the distribution shift of this kind. This can be observed in Fig. 10.

In summary, PnP-CoSMo produced generally equivalent or better reconstruction quality than the end-to-end methods despite its apparent handicap – i.e. completely ignoring the k-space training data and not being trained to explicitly solve the reconstruction problem. Moreover, this very feature of PnP-CoSMo makes it immune to contrast-related domain shifts. Finally, PnP-CoSMo was superior also to other plug-and-play methods, both unguided and guided ones, which share a similar design pattern and training data requirements.

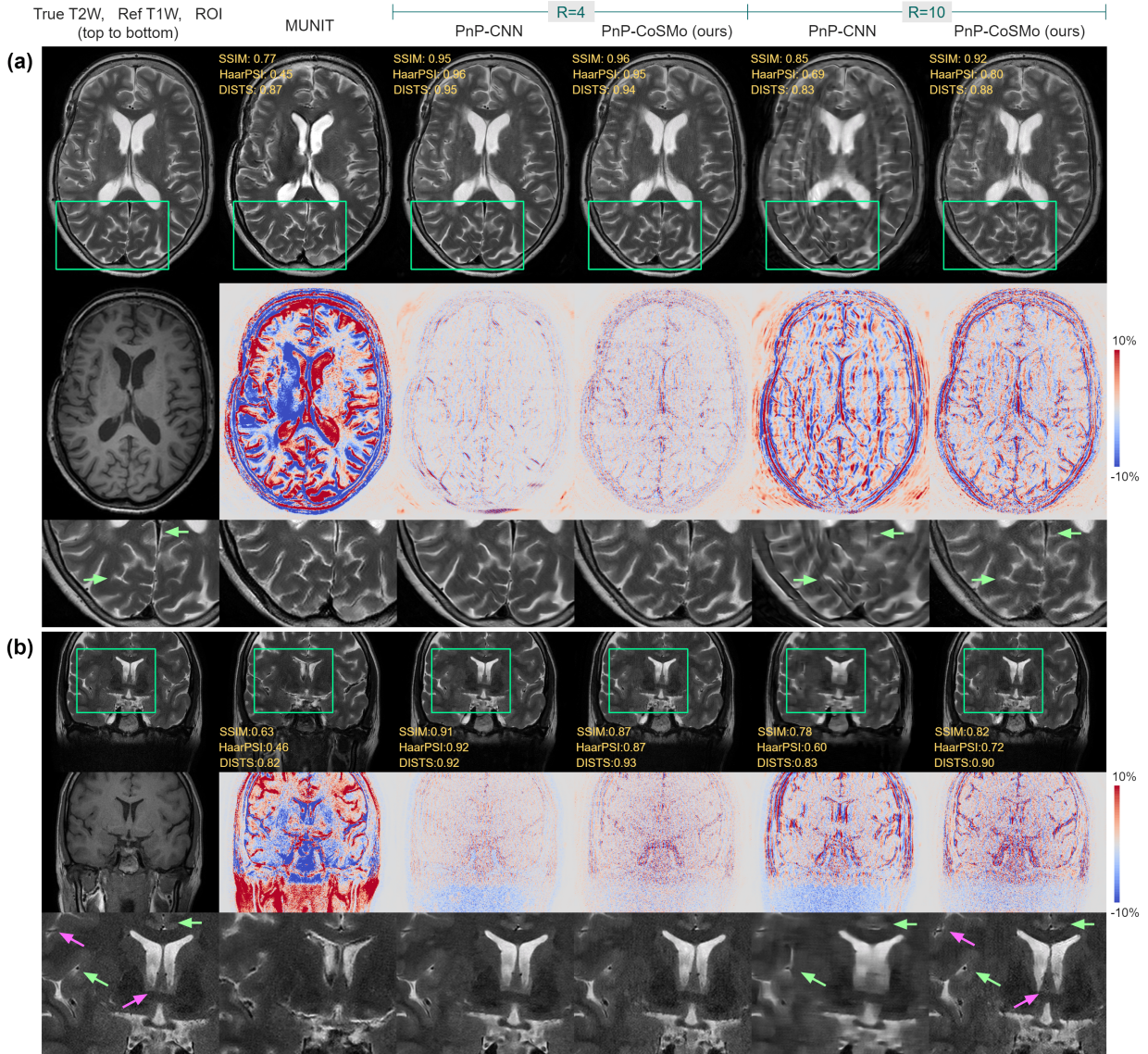


Figure 12: Sample slice from the *recon-test* sets of (a) LUMC-TRA and (b) LUMC-COR, comparing PnP-CoSMo reconstruction with PnP-CNN reconstruction and MUNIT image translation. MUNIT image translation produced severe anatomical defects, which is explained by its lack of access to k-space data. PnP-CoSMo, although comparable to PnP-CNN in quality at $R=4$, produced significantly sharper images at $R=10$, resolving many of the fine details (green arrows). In the LUMC-COR example, a curious case of model hallucination (magenta arrows) is also observed for PnP-CoSMo at $R=10$.

5.3. Benchmark and ablation on in-house LUMC multi-coil data

The LUMC datasets represent a more challenging problem with real-world data constraints. Additionally, in the light of the content capacity analysis (Section 5.1.2), we must note that the content capacity $J_M=1/4$ was optimal for the LUMC datasets, compared to NYU fastMRI DICOM data where $J_M=1$ was the optimal content capacity, which reflects a lower effective content information in the LUMC images and hence a greater difficulty of the guided reconstruction problem.

Fig. 11 plots the benchmark metrics for the LUMC test sets, which can be summarized in the following three trends. First, pure image translation with MUNIT was worse compared to single-contrast reconstruction, especially at lower acceleration factors (comparing with PnP-CNN, $p<0.05$ for all metrics and

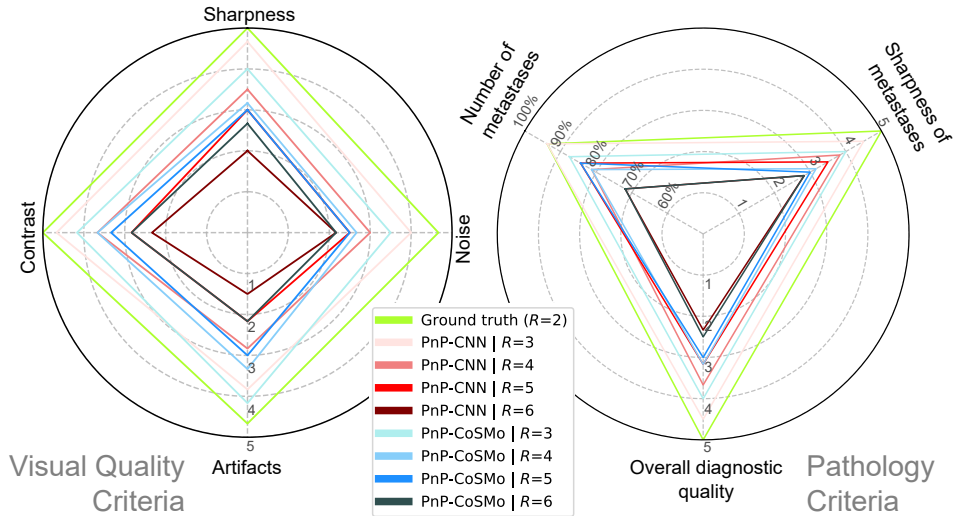


Figure 13: Aggregated scores from our preliminary radiological evaluation. At $R \in \{3, 4, 5\}$, PnP-CoSMo scored at least 3 on the Likert scale (fairly diagnostic quality), except for noise, while PnP-CNN was worse than fairly diagnostic in terms of artifacts at $R \in \{4, 5\}$ and tissue contrast at $R=5$. At these accelerations, both methods allowed the detection of at least 80% of the metastases. The main benefit of PnP-CoSMo over PnP-CNN is visible at the highest acceleration of $R=6$, showing a reduction in reconstruction artifacts and an improvement in tissue contrast, sharpness, and overall diagnostic quality.

both datasets). Combining it with L2-regularized reconstruction in PROSIT improved SSIM and HaarPSI ($p < 0.05$ for both datasets and accelerations), but not necessarily DISTS, suggesting that the available complementary information was not fully utilized. PnP-CoSMo was consistently better than both MUNIT image translation and PROSIT ($p < 0.05$ throughout for both cases). It also outperformed the conventional guided CS-STV ($p < 0.05$ throughout, except SSIM at $R=4$ in LUMC-COR). Hence, using both measured k-space and reference scan via PnP-CoSMo was more beneficial than (a) using either one of them and (b) combining both using hand-crafted priors, suggesting that our approach maximally exploits the complementary information. Second, both PnP-CNN and PnP-CoSMo performed similarly at lower acceleration, except in terms of SSIM and HaarPSI at $R=4$ and $R=6$ on LUMC-COR where PnP-CNN was slightly better. At higher acceleration, PnP-CoSMo outperformed PnP-CNN ($p < 0.05$ for all metrics and both datasets except SSIM at $R=8$ in LUMC-COR). Compared to PnP-CNN, PnP-CoSMo allowed up to 32.6% more acceleration for a given SSIM.² Third, introducing PFT and CR into the ablated PnP-CoSMo improved the reconstructions ($p < 0.05$ throughout in both cases except in DISTS for the latter at $R=10$ in LUMC-TRA). The contribution of PFT was almost constant across R , whereas that of CR decreased as R increased, which was expected since CR depends on the measured k-space data to refine the content.

Fig. 12 shows an LUMC-COR example representative of the first two trends. MUNIT image translation produced severe anatomical defects and predicted false structure in the lower region of the image where the ground truth, in fact, contains low signal. At $R=4$, PnP-CoSMo was visually similar to PnP-CNN, with the main difference being a blur effect in PnP-CNN and mild texture artifacts in PnP-CoSMo. At $R=10$, PnP-CNN reconstruction was non-viable, containing severe blur and artifacts (green arrows). On the other hand, PnP-CoSMo did not degrade much from the $R=4$ case and most fine structures were sharply resolved (green arrows). However, an interesting failure mode of PnP-CoSMo at high acceleration was the subtle localized distortions in the anatomy (magenta arrows).

5.4. Preliminary radiological evaluation

Fig. 13 plots the aggregated scores of our preliminary radiological evaluation and Fig. 14 shows a set of

²Based on linear interpolation of LUMC-TRA SSIM, PnP-CoSMo and PnP-CNN allowed $R=10$ and $R=6.7$, which is the maximum difference in R , at median SSIM=0.906. Hence, a difference of 32.6%.

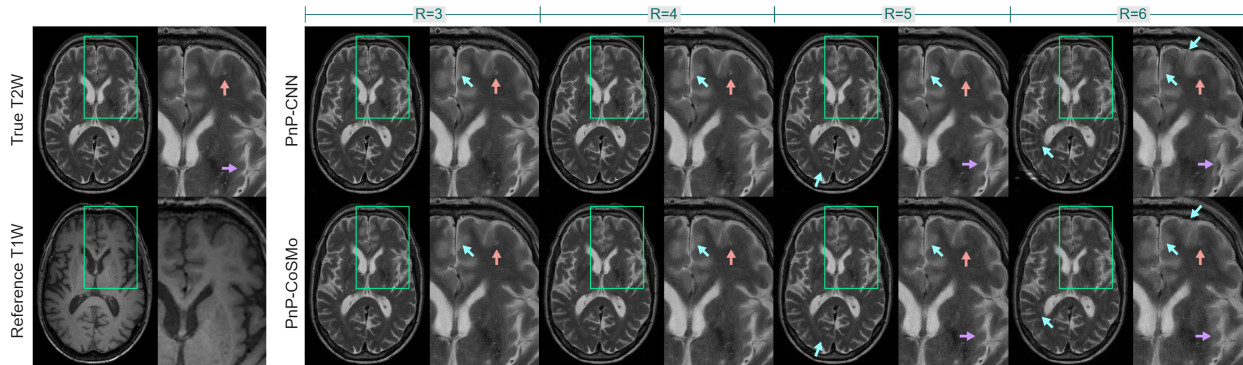


Figure 14: Example slice from an LUMC-TRA subject used in our preliminary radiological evaluation. PnP-CoSMo reconstructions had consistently less undersampling artifacts compared to PnP-CNN (cyan arrows), and had less blurring at $R \in \{5, 6\}$ (purple arrows). The pathological hyperintense feature (salmon-pink arrows) is prominently visible at $R=6$ in PnP-CoSMo, unlike in PnP-CNN where the local artifacts and the blurring interfere with its visibility.

representative example reconstructions.

At $R \in \{3, 4, 5\}$, PnP-CoSMo produced reconstructions of at least "fairly diagnostic" level (Likert score 3) of image sharpness, artifacts, tissue contrast, and overall diagnostic quality, while enabling the detection of at least 80% of all metastases. In terms of artifacts, PnP-CoSMo was consistently superior, as seen also in Fig. 14 (blue arrows). In terms of tissue contrast, it matched or exceeded PnP-CNN at $R \in \{4, 5, 6\}$ and produced sharper reconstructions at $R \in \{5, 6\}$ (purple arrows in Fig. 14). However, in terms of noise, it was equal or slightly worse. This may be explained by the difference in nature between the denoiser-type model of PnP-CNN and the more complex content/style model of PnP-CoSMo, potentially leading to noise-like grainy texture in the latter which also interferes with image sharpness and tissue contrast. In terms of the pathology criteria, while both algorithms scored similarly on the metastasis count, PnP-CoSMo had slightly better diagnostic quality at $R=6$. The general difference in reconstruction quality at $R=6$ can be seen in Fig. 14 where, compared to PnP-CoSMo, the PnP-CNN reconstruction shows severe reconstruction artifacts, blurrier and more distorted features (purple arrows), and a poorly visible hyperintense area of a brain metastasis (salmon-pink arrows).

In summary, both PnP-CoSMo and PnP-CNN allowed a maximum acceleration of $R=5$ for at least fairly diagnostic overall quality, i.e. with 60% less k-space samples than the clinical reconstructions of $R=2$. PnP-CoSMo was generally superior in terms of reconstruction artifacts and tissue contrast. Even at $R=6$, the highest acceleration considered here, the strong multi-contrast prior in PnP-CoSMo enabled sharper reconstructions (0.67 higher mean Likert score) with greater tissue contrast (0.5 higher), less artifacts (0.67 higher), and higher overall diagnostic quality (0.17 higher) compared to the PnP-CNN baseline. The assessment by the two observers agreed with a Spearman's rank correlation coefficient of 0.81 for the Likert-scale scores and 0.98 for the metastasis count.

6. Discussion

In this work, we modeled two-contrast MR image data in terms of two latent generative factors – *content* representing the contrast-independent structure and *style* representing the contrast-specific variations. Our data-driven definitions of content and style, though seemingly related to the MR physics-based representations of quantitative maps and acquisition-related factors, are rather nebulous compared to precisely defined physical concepts. For instance, MR quantitative maps are theoretically objective representations of tissues in terms of physical variables such as relaxation times and are ideally independent of the contrast-generating sequence parameters. On the other hand, our content and style representations are only defined statistically in terms of the given two contrasts and are, thus, neither as objective nor as independent in the ideal physical sense. That being said, we would argue that there is potential value in augmenting the data-driven content/style model with MR physical models, e.g. by constraining the learned content to represent physically

meaningful anatomical properties, introducing elements of a physical model (e.g. Bloch equations) into the decoder network, etc., to enhance interpretability and reconstruction quality.

Optimal content capacity (Section 3.2.3) was defined as a quantity representing the amount of shared local information contained in a two-contrast dataset. In terms of this quantity, we analyzed the effect of reference image resolution on reconstruction quality, obtaining a lowerbound for PnP-CoSMo to be effective (Section 5.1.2), specifically a reference resolution $1/8^{\text{th}}$ of the target image resolution, corresponding to $J_M=1/16^{\text{th}}$ of the total spatial information in the target. This quantity would depend on more fundamental factors such as MR sequence types, which we did not investigate here. While we limited our experiments to T1W and T2W sequences, PnP-CoSMo is, in principle, applicable to any pair of contrasts, with the image quality limited mainly by the amount of structural information shared between them. Future work could help empirically determine which sequence pairs are more amenable to guided reconstruction than others.

A consequence of our MUNIT-based model design was the model’s lack of dependence on the unidirectionality of the guided reconstruction problem, which allowed greater generalizability by design (Section 5.2). It is, in principle, also possible to model the content and style for more than two contrasts. This would enable not only the generalizability of our approach to any combinatorial set of guided reconstruction tasks, but also better estimation of the target contrast’s content by utilizing multiple reference contrasts in the reconstruction. Given number of contrasts N , content could be defined as the local structure underlying all these contrasts, while style would encode intra-contrast variations of each individual contrast. This model would then require an (unpaired) image-domain training dataset of the N contrasts. An open question is how to effectively scale the model and training complexity to N contrasts. The PnP-CoSMo algorithm can subsequently be extended to utilize multiple reference contrasts to guide a given target contrast. The specific question to investigate then would be – given P reference contrasts (where $1 < P < N$), how to aggregate their contents such that the prior structural information about the target image is maximized?

Content discrepancy (Section 3.3) was characterized as a quantity representing the gap between the true content of the target image and our estimation of this content, which is another limiting factor in PnP-CoSMo reconstruction. In our MUNIT-based network design, the decoders model the (forward) generative process that maps the latent variables (i.e. content and style) to the observable variable (i.e. images). Ideally, the encoders must be a perfect inverse of this forward process. However, estimating the multi-channel contrast-independent content from a single image (using the content encoders) is a challenging (and perhaps ill-conditioned) inverse problem. Hence, some errors are to be expected in the content estimated from the reference image. Moreover, the reference image may contain unfavorable differences from the target image, such as misalignment or artifacts, which introduce more errors. Therefore, content discrepancy is expected to be a non-zero quantity. We proposed two complementary ways to minimize its effect on the reconstruction. While paired fine-tuning improves the model using a small amount of paired image-domain training data, content refinement (CR) aims to correct the remaining discrepancy during reconstruction using the measured k -space. A drawback of the CR module, however, is slower convergence (Section 5.1.3). For example, the run-time for PnP-CoSMo on the GPU was around 17 seconds for a slice of matrix size 349×284 , as compared to 6 seconds for CS-WT, 1.4 seconds for PnP-CNN, and less than 0.1 second for MC-VarNet. This latency issue could be mitigated by approximating the iterative process with an unrolled network design, although potentially at a cost of the generalizability offered by the plug-and-play design. The resulting trade-off between model latency and generalizability would be interesting to explore in the future.

In terms of training data requirements, PnP-CoSMo can make use of the larger amounts of the available image-domain data and can be applied to situations where end-to-end methods are infeasible. In situations where end-to-end methods are indeed feasible, such as in our NYU fastMRI benchmark (Section 5.2), PnP-CoSMo was often superior to state-of-the-art unguided (MoDL) and guided (MC-VarNet and MTrans) networks in terms of both metrics and visual quality, especially at higher accelerations, e.g. at $R=5$ with a difference of 0.01 SSIM, 0.04 HaarPSI, and 0.02 DISTS on average over MC-VarNet in Task-1 and of 0.01 SSIM, 0.08 HaarPSI, and 0.04 DISTS in Task-2, despite PnP-CoSMo *completely ignoring the k -space training data and not being explicitly optimized for any reconstruction task in the training phase*. Additionally, PnP-CoSMo is, by design, immune to cross-contrast distribution shifts as opposed to end-to-end methods, which was demonstrated, e.g. in comparison with MC-VarNet which suffered a difference of up to 0.10 SSIM,

0.17 HaarPSI, and 0.06 DISTS on average when applied on out-of-distribution tasks. Compared to other plug-and-play methods, which share a similar de-coupled design pattern and the image-only training data requirement as PnP-CoSMo, it produced sharper and higher-fidelity reconstructions and higher metrics, e.g. with a maximum difference of 0.05 SSIM, 0.13 HaarPSI, and 0.03 DISTS on average over PROSIT in Task-1 and of 0.03 SSIM, 0.10 HaarPSI, and 0.02 DISTS in Task-2. Moreover, the *unpaired* image-domain pre-training of the content/style model boosts the practical applicability of PnP-CoSMo, e.g. in the case of LUMC-TRA where the T1W/T2W image data imbalance was considerable (Table 2). In our LUMC multi-coil benchmark, we limited our baselines to those algorithms that were feasible given the data constraint. As future work, a more comprehensive study should be conducted with a broader range of methods and evaluation criteria, e.g. comparing generalizability across accelerations and sampling patterns with multi-contrast unrolled networks, given a fixed budget of paired training data. Contrary to the training stage, we strictly assumed the spatial alignment of the reference and target images in the reconstruction stage. The CR module, which can implicitly correct minor registration errors, would likely break down at the typically observed levels of patient motion. A potential solution is to incorporate an online registration step to explicitly and efficiently correct for arbitrary inter-scan motion, thereby further improving practical applicability.

In terms of reconstruction quality on multi-coil data, we observed in Section 5.3 that the true added value of PnP-CoSMo was at the high acceleration factors ($R \in \{8, 10\}$) where the k-space data is scarce and the reference information becomes more valuable. For example, at $R=10$ and compared to PnP-CNN, PnP-CoSMo showed an improvement of 0.04 SSIM, 0.08 HaarPSI, and 0.05 DISTS on LUMC-TRA and of 0.02 SSIM, 0.12 HaarPSI, and 0.09 DISTS on LUMC-COR. However, the risk of model hallucinations increases at these extreme accelerations, raising concerns about the accuracy of the anatomy represented in the image. We hypothesize that as a consequence of content/style decomposition, it may be possible to leverage the contrast-independence property of the content to – (a) automatically detect local hallucinations in the reconstruction and (b) define a corrective process in combination with an adaptive sampling strategy to minimize it. This is yet another topic for future work. At lower accelerations, on the other hand, we observed that PnP-CoSMo often produced slightly lower metrics compared to PnP-CNN, e.g. in LUMC-COR. This was also observed in our preliminary radiological evaluation on LUMC-TRA samples (Section 5.4), with PnP-CoSMo reconstructions at $R \in \{3, 4\}$ containing noise-like grainy texture which also interfered with criteria such as sharpness. At first glance, this is counter-intuitive since PnP-CoSMo has access to additional side information and should, in principle, perform at least as well as PnP-CNN. However, this can be explained by the fact that at lower accelerations, the quality of the content/style model M becomes the main limiting factor for reconstruction quality. This is because unlike the CNN denoiser (Eq. (4)) of PnP-CNN, the content consistency operator $g_M(\cdot, c)$ (Eq. (15)) of PnP-CoSMo radically alters the image and hence, this operation is sensitive to the model’s overall performance. The model performance is in turn influenced by the training dataset and the network architecture. First, regarding data, the T1W scans in LUMC datasets had an in-plane resolution 1.3-2.5 times lower than that of the T2W scans, limiting the quality of the model (as indicated by its low optimal content capacity) and the overall value of guidance. In the long run, this may be solved by using 3D reference and target sequences of matched-resolution to optimize guidance. Second, regarding model design, correcting for content discrepancy using the CR module relies on computing gradients through the decoder G_2 (Eq. (17)). If G_2 is highly non-linear and the reference content is not sufficiently close to the optimum, CR may converge to a sub-optimal point leading to grainy texture in the reconstruction, e.g. as seen in Fig. 12 at $R=4$. In our proof-of-concept, we used the same general model architecture proposed in Huang et al. (2018). Better designs that are more conducive to CR may be possible. Hence, future efforts will focus considerably on improving the content/style model using specialized architecture and regularization.

Finally, our preliminary radiological study demonstrated that (a) PnP-CoSMo was comparable with non-guided PnP-CNN in delivering at least fairly diagnostic overall quality (Likert score 3) reconstructions at $R=5$, i.e. with 60% less k-space samples than the current clinical protocol of $R=2$ and (b) PnP-CoSMo’s content/style modeling effectively leveraged reference contrast information enabling reconstructions with greater sharpness and tissue contrast, less artifacts, and a higher overall diagnostic quality at $R=6$, with an improvement of 0.67, 0.5, 0.67, and 0.17 mean Likert scores, respectively. As a supplementary component

to our LUMC multi-coil benchmark, this preliminary evaluation provides an early indication of potential benefit in the clinic, particularly time-saving during acquisition. Given the limited scale of our current evaluation, however, a large-scale clinical validation involving larger sample size and multiple radiologists must be conducted to robustly gauge the clinical utility of our approach. Such a clinical validation was beyond the scope of our current technical work and is, hence, a topic for a clinically-focused future work.

7. Conclusion

In this work, we introduced PnP-CoSMo, a modular approach to multi-contrast reconstruction which combines content/style modeling with iterative reconstruction, offering the reconstruction quality of state-of-the-art end-to-end methods with improved cross-contrast generalizability despite not requiring any k-space training data. At its core is the content consistency operation, which provides regularization at the semantic level of the image content. We defined two quantities that determine the efficacy of this operation, namely optimal content capacity and content discrepancy, and provided several ways of maximizing this efficacy. On real-world clinical data, PnP-CoSMo provided up to 32.6% more acceleration over PnP-CNN for given SSIM, enabling sharper reconstructions at high accelerations. In our preliminary radiological task of visual quality assessment and brain metastasis diagnosis at realistic accelerations, PnP-CoSMo produced images of at least fairly diagnostic overall quality at $R=5$, enabling 60% more acceleration over clinical reconstructions. To progress from our current proof-of-concept towards a practical implementation, future work will focus mainly on improving and extending the content/style model, reducing reconstruction latency, tackling the problem of model hallucinations, incorporating online registration, and conducting a large-scale radiological study.

CRedit authorship contribution statement

Chinmay Rao: Conceptualization, Methodology, Data curation, Software, Investigation, Validation, Formal analysis, Visualization, Writing – original draft. **Matthias van Osch:** Funding acquisition, Supervision, Conceptualization, Validation, Writing – review & editing. **Nicola Pezzotti:** Funding acquisition, Supervision, Conceptualization, Methodology, Validation. **Jeroen de Bresser:** Investigation, Validation. **Mark van Buchem:** Investigation, Validation. **Laurens Beljaards:** Data curation, Software. **Jakob Meineke:** Resources, Software. **Elwin de Weerd:** Conceptualization, Resources. **Huangling Lu:** Investigation. **Mariya Doneva:** Supervision, Conceptualization, Methodology, Validation, Writing – review & editing. **Marius Staring:** Funding acquisition, Project administration, Supervision, Conceptualization, Methodology, Validation, Writing – review & editing.

Declaration of competing interest

The authors declare the following financial interests or personal relationships which may be considered as potential competing interests: Chinmay Rao and Laurens Beljaards declare the grant and research support they receive from Philips. Nicola Pezzotti, Jakob Meineke, Elwin de Weerd, and Mariya Doneva declare their employment at Philips. If there are other authors, they declare that they have no known competing financial interests or personal relationships that could have appeared to influence the work reported in this paper.

Acknowledgments

This work is part of the project ROBUST: Trustworthy AI-based Systems for Sustainable Growth with project number KICH3.LTP.20.006, which is (partly) financed by the Dutch Research Council (NWO), Philips Research, and the Dutch Ministry of Economic Affairs and Climate Policy (EZK) under the program LTP KIC 2020-2023.

Data availability

The authors do not have permission to share data.

References

- Aggarwal, H.K., Mani, M.P., Jacob, M., 2018. MoDL: Model-based deep learning architecture for inverse problems. *IEEE Trans. Med. Imaging* 38, 394–405. <https://doi.org/10.1109/TMI.2018.2865356>.
- Ahmad, R., Bouman, C.A., Buzzard, G.T., Chan, S., Liu, S., Reehorst, E.T., Schniter, P., 2020. Plug-and-play methods for magnetic resonance imaging using denoisers for image recovery. *IEEE Signal Process. Mag.* 37, 105–116. <https://doi.org/10.1109/MSP.2019.2949470>.
- Atli, O.F., Kabas, B., Arslan, F., Demirtas, A.C., Yurt, M., Dalmaz, O., Çukur, T., 2024. I2I-Mamba: Multi-modal medical image synthesis via selective state space modeling. *arXiv preprint arXiv:2405.14022* <https://doi.org/10.48550/arXiv.2405.14022>.
- Bilgic, B., Goyal, V.K., Adalsteinsson, E., 2011. Multi-contrast reconstruction with Bayesian compressed sensing. *Magn. Reson. Med.* 66, 1601–1615. <https://doi.org/10.1002/mrm.22956>.
- Boyd, S., Parikh, N., Chu, E., Peleato, B., Eckstein, J., et al., 2011. Distributed optimization and statistical learning via the alternating direction method of multipliers. *Found. Trends Mach. Learn.* 3, 1–122. <https://doi.org/10.1561/22000000016>.
- Chambolle, A., De Vore, R.A., Lee, N.Y., Lucier, B.J., 1998. Nonlinear wavelet image processing: Variational problems, compression, and noise removal through wavelet shrinkage. *IEEE Trans. Image Process.* 7, 319–335. <https://doi.org/10.1109/83.661182>.
- Collins, D.L., Zijdenbos, A.P., Kollokian, V., Sled, J.G., Kabani, N.J., Holmes, C.J., Evans, A.C., 1998. Design and construction of a realistic digital brain phantom. *IEEE Trans. Med. Imaging* 17, 463–468. <https://doi.org/10.1109/42.712135>.
- Dar, S.U., Yurt, M., Karacan, L., Erdem, A., Erdem, E., Çukur, T., 2019. Image synthesis in multi-contrast MRI with conditional generative adversarial networks. *IEEE Trans. Med. Imaging* 38, 2375–2388. <https://doi.org/10.1109/TMI.2019.2901750>.
- Dar, S.U., Yurt, M., Shahdloo, M., Ildız, M.E., Tmaz, B., Çukur, T., 2020. Prior-guided image reconstruction for accelerated multi-contrast MRI via generative adversarial networks. *IEEE J. Sel. Top. Signal Process.* 14, 1072–1087. <https://doi.org/10.1109/JSTSP.2020.3001737>.
- Denck, J., Guehring, J., Maier, A., Rothgang, E., 2021. MR-contrast-aware image-to-image translations with generative adversarial networks. *Int. J. Comput. Assist. Radiol. Surg.* 16. <https://doi.org/10.1007/s11548-021-02433-x>.
- Ehrhardt, M.J., Betcke, M.M., 2016. Multicontrast MRI reconstruction with structure-guided total variation. *SIAM J. Imaging Sci.* 9, 1084–1106. <https://doi.org/10.1137/15M1047325>.
- Feng, C.M., Yan, Y., Chen, G., Xu, Y., Hu, Y., Shao, L., Fu, H., 2022. Multimodal transformer for accelerated MR imaging. *IEEE Trans. Med. Imaging* 42, 2804–2816. <https://doi.org/10.1109/TMI.2022.3180228>.
- Griswold, M.A., Jakob, P.M., Heidemann, R.M., Nittka, M., Jellus, V., Wang, J., Kiefer, B., Haase, A., 2002. Generalized autocalibrating partially parallel acquisitions (GRAPPA). *Magn. Reson. Med.* 47, 1202–1210. <https://doi.org/10.1002/mrm.10171>.
- Huang, J., Chen, C., Axel, L., 2014. Fast multi-contrast MRI reconstruction. *Magn. Reson. Imaging* 32, 1344–1352. <https://doi.org/10.1016/j.mri.2014.08.025>.

- Huang, X., Liu, M.Y., Belongie, S., Kautz, J., 2018. Multimodal unsupervised image-to-image translation, in: European Conference on Computer Vision (ECCV), Springer-Verlag, Berlin, Heidelberg. p. 179–196. https://doi.org/10.1007/978-3-030-01219-9_11.
- Isola, P., Zhu, J.Y., Zhou, T., Efros, A.A., 2017. Image-to-image translation with conditional adversarial networks, in: 2017 IEEE Conference on Computer Vision and Pattern Recognition (CVPR), pp. 5967–5976. <https://doi.org/10.1109/CVPR.2017.632>.
- Kamilov, U.S., Bouman, C.A., Buzzard, G.T., Wohlberg, B., 2023. Plug-and-play methods for integrating physical and learned models in computational imaging: Theory, algorithms, and applications. *IEEE Signal Process. Mag.* 40, 85–97. <https://doi.org/10.1109/MSP.2022.3199595>.
- Kastryulin, S., Zakirov, J., Pezzotti, N., Dylov, D.V., 2023. Image quality assessment for magnetic resonance imaging. *IEEE Access* 11, 14154–14168. <https://doi.org/10.1109/ACCESS.2023.3243466>.
- Klein, S., Staring, M., Murphy, K., Viergever, M.A., Pluim, J.P., 2009. Elastix: A toolbox for intensity-based medical image registration. *IEEE Trans. Med. Imaging* 29, 196–205. <https://doi.org/10.1109/TMI.2009.2035616>.
- Knoll, F., Zbontar, J., Sriram, A., Muckley, M.J., Bruno, M., Defazio, A., Parente, M., Geras, K.J., Katsnelson, J., Chandarana, H., et al., 2020. fastMRI: A publicly available raw k-space and DICOM dataset of knee Images for accelerated MR image reconstruction using machine learning. *Radiol.: Artif. Intell.* 2, e190007. <https://doi.org/10.1148/ryai.2020190007>.
- Kopanoglu, E., Güngör, A., Kilic, T., Saritas, E.U., Oguz, K.K., Çukur, T., Güven, H.E., 2020. Simultaneous use of individual and joint regularization terms in compressive sensing: Joint reconstruction of multi-channel multi-contrast MRI acquisitions. *NMR Biomed.* 33, e4247. <https://doi.org/10.1002/nbm.4247>.
- Kotovenko, D., Sanakoyeu, A., Lang, S., Ommer, B., 2019. Content and style disentanglement for artistic style transfer, in: 2019 IEEE/CVF International Conference on Computer Vision (ICCV), pp. 4421–4430. <https://doi.org/10.1109/ICCV.2019.00452>.
- Kwon, G., Ye, J.C., 2021. Diagonal attention and style-based GAN for content-style disentanglement in image generation and translation, in: 2021 IEEE/CVF International Conference on Computer Vision (ICCV), pp. 13960–13969. <https://doi.org/10.1109/ICCV48922.2021.01372>.
- Lei, P., Fang, F., Zhang, G., Zeng, T., 2023. Decomposition-based variational network for multi-contrast MRI super-resolution and reconstruction, in: 2023 IEEE/CVF International Conference on Computer Vision (ICCV), pp. 21239–21249. <https://doi.org/10.1109/ICCV51070.2023.01947>.
- Levac, B., Jalal, A., Ramchandran, K., Tamir, J.I., 2023. MRI reconstruction with side information using diffusion models, in: 2023 57th Asilomar Conference on Signals, Systems, and Computers, IEEE. pp. 1436–1442. <https://doi.org/10.1109/IEEECONF59524.2023.10476807>.
- Liu, M.Y., Breuel, T., Kautz, J., 2017. Unsupervised image-to-image translation networks, in: Guyon, I., Luxburg, U.V., Bengio, S., Wallach, H., Fergus, R., Vishwanathan, S., Garnett, R. (Eds.), *Advances in Neural Information Processing Systems (NeurIPS)*, Curran Associates, Inc.
- Liu, X., Wang, J., Lin, S., Crozier, S., Liu, F., 2021a. Optimizing multicontrast MRI reconstruction with shareable feature Aggregation and selection. *NMR Biomed.* 34, e4540. <https://doi.org/10.1002/nbm.4540>.
- Liu, X., Wang, J., Sun, H., Chandra, S.S., Crozier, S., Liu, F., 2021b. On the regularization of feature fusion and mapping for fast MR multi-contrast imaging via iterative networks. *Magn. Reson. Imaging* 77, 159–168. <https://doi.org/10.1016/j.mri.2020.12.019>.

- Lustig, M., Donoho, D., Pauly, J.M., 2007. Sparse MRI: The application of compressed sensing for rapid MR imaging. *Magn. Reson. Med.* 58, 1182–1195. <https://doi.org/10.1002/mrm.21391>.
- Mason, A., Rioux, J., Clarke, S.E., Costa, A., Schmidt, M., Keough, V., Huynh, T., Beyea, S., 2019. Comparison of objective image quality metrics to expert radiologists’ scoring of diagnostic quality of MR images. *IEEE Trans. Med. Imaging* 39, 1064–1072. <https://doi.org/10.1109/TMI.2019.2930338>.
- Mattern, H., Sciarra, A., Dünnwald, M., Chatterjee, S., Müller, U., Oetze-Jafra, S., Speck, O., 2020. Contrast prediction-based regularization for iterative reconstructions (PROSIT), in: *International Society for Magnetic Resonance in Medicine (ISMRM)*.
- Miyato, T., Kataoka, T., Koyama, M., Yoshida, Y., 2018. Spectral normalization for generative adversarial networks. *arXiv preprint arXiv:1802.05957* <https://doi.org/10.48550/arXiv.1802.05957>.
- Oh, G., Sim, B., Chung, H., Sunwoo, L., Ye, J.C., 2020. Unpaired deep learning for accelerated MRI using optimal transport driven CycleGAN. *IEEE Trans. Comput. Imaging* 6, 1285–1296. <https://doi.org/10.1109/TCI.2020.3018562>.
- Pezzotti, N., Yousefi, S., Elmahdy, M.S., Van Gemert, J.H.F., Schuelke, C., Doneva, M., Nielsen, T., Kastrulyin, S., Lelieveldt, B.P.F., Van Osch, M.J.P., De Weerd, E., Staring, M., 2020. An adaptive intelligence algorithm for undersampled knee MRI reconstruction. *IEEE Access* 8, 204825–204838. <https://doi.org/10.1109/ACCESS.2020.3034287>.
- Pooja, K., Ramzi, Z., Chaithya, G., Ciuciu, P., 2022. MC-PDNet: Deep unrolled neural network for multi-contrast MR image reconstruction from undersampled k-space data, in: *2022 IEEE 19th International Symposium on Biomedical Imaging (ISBI)*, pp. 1–5. <https://doi.org/10.1109/ISBI52829.2022.9761583>.
- Pruessmann, K.P., Weiger, M., Börner, P., Boesiger, P., 2001. Advances in sensitivity encoding with arbitrary k-space trajectories. *Magn. Reson. Med.* 46, 638–651. <https://doi.org/10.1002/mrm.1241>.
- Rao, C., Beljaards, L., van Osch, M., Doneva, M., Meineke, J., Schuelke, C., Pezzotti, N., de Weerd, E., Staring, M., 2024. Guided multicontrast reconstruction based on the decomposition of content and style, in: *International Society for Magnetic Resonance in Medicine (ISMRM)*.
- Richardson, E., Weiss, Y., 2021. The surprising effectiveness of linear unsupervised image-to-image translation, in: *2020 25th International Conference on Pattern Recognition (ICPR)*, pp. 7855–7861. <https://doi.org/10.1109/ICPR48806.2021.9413199>.
- Schlemper, J., Caballero, J., Hajnal, J.V., Price, A.N., Rueckert, D., 2017. A deep cascade of convolutional neural networks for dynamic MR image reconstruction. *IEEE Trans. Med. Imaging* 37, 491–503. <https://doi.org/10.1109/TMI.2017.2760978>.
- Seow, P., Kheok, S.W., Png, M.A., Chai, P.H., Yan, T.S.T., Tan, E.J., Liauw, L., Law, Y.M., Anand, C.V., Lee, W., et al., 2024. Evaluation of compressed SENSE on image quality and reduction of MRI acquisition time: A clinical validation study. *Acad. Radiol.* 31, 956–965. <https://doi.org/10.1016/j.acra.2023.07.013>.
- Song, P., Weizman, L., Mota, J.F.C., Eldar, Y.C., Rodrigues, M.R.D., 2020. Coupled dictionary learning for multi-contrast MRI reconstruction. *IEEE Trans. Med. Imaging* 39, 621–633. <https://doi.org/10.1109/TMI.2019.2932961>.
- Wang, Q., Wen, Z., Shi, J., Wang, Q., Shen, D., Ying, S., 2024. Spatial and modal optimal transport for fast cross-modal MRI reconstruction. *IEEE Trans. Med. Imaging* 43, 3924–3935. <https://doi.org/10.1109/TMI.2024.3406559>.

- Weizman, L., Eldar, Y.C., Ben Bashat, D., 2016. Reference-based MRI. *Med. Phys.* 43, 5357–5369. <https://doi.org/10.1118/1.4962032>.
- Wu, Y., Nakashima, Y., Garcia, N., 2023. Not only generative art: Stable diffusion for content-style disentanglement in art analysis, in: *Proceedings of the 2023 ACM International Conference on Multimedia Retrieval*, Association for Computing Machinery, New York, NY, USA. p. 199–208. <https://doi.org/10.1145/3591106.3592262>.
- Xuan, K., Xiang, L., Huang, X., Zhang, L., Liao, S., Shen, D., Wang, Q., 2022. Multimodal mri reconstruction assisted with spatial alignment network. *IEEE Trans. Med. Imaging* 41, 2499–2509. <https://doi.org/10.1109/TMI.2022.3164050>.
- Yang, Y., Wang, N., Yang, H., Sun, J., Xu, Z., 2020. Model-driven deep attention network for ultra-fast compressive sensing MRI uided by cross-contrast MR image, in: Martel, A.L., et al. (eds) *Medical Image Computing and Computer Assisted Intervention – MICCAI 2020*. MICCAI 2020. Lecture Notes in Computer Science, vol 12262, Springer, Cham. pp. 188–198. https://doi.org/10.1007/978-3-030-59713-9_19.
- Yurt, M., Dar, S.U., Erdem, A., Erdem, E., Oguz, K.K., Çukur, T., 2021. mustGAN: Multi-stream generative adversarial networks for MR image synthesis. *Med. Image Anal.* 70, 101944. <https://doi.org/10.1016/j.media.2020.101944>.
- Zbontar, J., Knoll, F., Sriram, A., Murrell, T., Huang, Z., Muckley, M., Defazio, A., Stern, R., Johnson, P., Bruno, M., et al., 2018. fastMRI: An open dataset and benchmarks for accelerated MRI. *arXiv preprint arXiv:1811.08839* <https://doi.org/10.48550/arXiv.1811.08839>.
- Zhou, B., Zhou, S.K., 2020. DuDoRNet: Learning a dual-domain recurrent network for fast MRI reconstruction with deep T1 prior, in: *2020 IEEE/CVF Conference on Computer Vision and Pattern Recognition (CVPR)*, pp. 4272–4281. <https://doi.org/10.1109/CVPR42600.2020.00433>.
- Zhu, J.Y., Park, T., Isola, P., Efros, A.A., 2017. Unpaired image-to-image translation using cycle-consistent adversarial networks, in: *2017 IEEE International Conference on Computer Vision (ICCV)*, pp. 2242–2251. <https://doi.org/10.1109/ICCV.2017.244>.